Coregistration of heading to visual cues in retrosplenial cortex

Kevin K. Sit[1] and Michael J. Goard[1, 2, 3, *]

[1]Department of Psychological and Brain Sciences
University of California, Santa Barbara
Santa Barbara, CA, 93106, USA

[2]Department of Molecular, Cellular, and Developmental Biology
University of California, Santa Barbara
Santa Barbara, CA, 93106, USA

[3]Neuroscience Research Institute
University of California Santa Barbara
Santa Barbara, CA, 93106, USA

[*]Correspondence to: michael.goard@lifesci.ucsb.edu

Abstract

Spatial cognition depends on an accurate representation of orientation within an environment. Head direction cells in distributed brain regions receive a range of sensory inputs, but visual input is particularly important for aligning their responses to environmental landmarks. To investigate how population-level heading responses are aligned to visual input, we recorded from retrosplenial cortex (RSC) of head-fixed mice in a moving environment using two-photon calcium imaging. We show that RSC neurons are tuned to the animal's relative orientation in the environment, even in the absence of head movement. Next, we found that RSC receives functionally distinct projections from visual and thalamic areas, and contains several functional classes of neurons. While some functional classes mirror RSC inputs, a newly discovered class coregisters visual and thalamic signals. Finally, decoding analyses reveal unique contributions to heading from each class. Our results suggest an RSC circuit for anchoring heading representations to environmental visual landmarks.

Introduction

A sense of direction is essential for animals to accurately perceive and move through their environment. Rather than being coupled to absolute coordinates, such as magnetic north, direction is represented in the brain as the relative orientation of an animal in its current environment, termed "heading". Although heading and head direction are generally aligned in a freely moving animal, they can be experimentally decoupled when head movement and environmental movement are independent. For example, researchers have observed heading responses in insects that track the movement of a virtual environment even with the head immobilized [1–3].

A distributed network [4–8] of head direction (HD) neurons found throughout the mammalian brain represent direction through increased firing when an animal's head is in a specific orientation relative to the environment [4, 9–12]. A central hub of this network is the anterodorsal thalamic nucleus (ADN), which contains a high percentage of HD neurons and is crucial for navigation [4, 12–14]. Early investigations of responses in the HD cell network demonstrated that the vestibular system plays a critical role in both the generation and maintenance of HD neurons. Lesions of the vestibular system, either in sensory organs [15–17] or in upstream relay nuclei [18, 19], degrade the responses of HD neurons in ADN and other regions in the HD cell network, resulting in navigational deficits. Although HD cell responses have been observed in

restrained rodents in virtual environments, all experiments to this point have involved physical head rotation, either animal-controlled [**Chen2018**, 20, 21] or experimenter-controlled [22–24]. Despite the importance of vestibular input, previous work has shown that the visual system, though not necessary for the generation of HD cell responses responses, plays a crucial role in anchoring the responses to cues in the external environment [4, 10, 22, 25]. Experiments which remove visual information by recording from animals in darkness, have shown that HD neuron firing gradually drifts from the animal's physical head direction over time [10, 25]. Moreover, turning on the lights results in a nearly instantaneous realignment of HD cell responses to visual cues, even if the cues were inconspicuously moved in the darkness, suggesting that visual information exerts a dominating influence on representations, supplanting cues from other sensory systems [26]. Indeed, behavioral experiments in several species that either dampen or remove vestibular information have shown that animals are still capable of successful navigation through the use of visual landmarks alone [1, 16, 27–29]; though other sensory inputs, such as optic flow [21, 30], proprioception [31], motor efference copy [32], and olfaction [33] also contribute. Although visual input is known to play a critical role in registering heading representations to the environment, the mechanism of alignment has not been fully elucidated.

Recent research has suggested that the retrosplenial cortex (RSC), a cortical region in the HD cell network, may play an important role in the integration of these signals [6, 7]. Lesioning RSC degrades HD cell responses in ADN [34, 35], suggesting that RSC directly contributes to HD cell tuning, which is further supported by reciprocal projections from RSC to ADN [36–39]. Furthermore, RSC is one of only two principal areas, the other being the postsubiculum [36, 37], that receives direct innervation from both the visual cortex and the ADN. RSC also has important roles in navigation, particularly regarding landmark detection [40–45] and path integration [46, 47], and has been shown to integrate visual information with vestibular input in the angular head velocity (AHV) system [48]. Finally, in the presence of conflicting visual landmarks, individual HD neurons in RSC exhibit multimodal tuning curves that capture the angular offset with respect to each landmark, suggesting that RSC can represent and resolve this ambiguity [43, 49]. These findings suggest that RSC is uniquely situated to receive and integrate sensory information from visual system into a unified representation of heading. Here, we use 2-photon calcium imaging of RSC cell bodies and axonal inputs to investigate how visual cues are used to register heading to the external environment.

Results

Neurons in the RSC represent heading in the absence of physical head movements

In order to investigate the interaction of visual input and heading using 2-photon imaging of somata and axon terminals, we developed a preparation in which mice are head restrained in a moving environment (Figure 1A). To clarify our terminology, in previous studies the relative orientation of the head to the environment was generally determined by physical movement of the animal's head in a stationary environment, leading to the term "head direction cells". Since our experiments have the head immobilized, we define tuned neurons as "heading" cells, since they represent the relative orientation of the stationary head to a moving environment. Heading responses have been found in invertebrates in preparations in which the head is immobilized [1–3], but to date all experiments investigating HD cells in mammals have incorporated physical head movement [**Chen2018**, 20, 21]. Virtual reality systems [**Chen2018**, 50–52] are commonly used for navigation tasks in head-fixed preparations, but have some significant drawbacks, such as a lack of depth cues, somatosensory feedback, and limited proprioceptive input. To address these limitations, we opted to use a walled circular chamber that floats on an air table [53], and contains an array of sensors to collect measurements from the chamber, including linear position, angular orientation, and speed (Figure 1A, D, see Methods). This approach holds vestibular input constant, while allowing the mice to experience the visual and proprioceptive inputs associated with movement relative to the environment.

To determine if mammalian RSC neurons show tuning for heading even when the head is stationary, we allowed head-fixed mice to ambulate within a floating chamber while simultaneously imaging from the posterior dysgranular RSC ($n = 4$ recordings over 3 mice, Figure 1B). Posterior dysgranular RSC was chosen because it receives direct projections from visual cortex [38, 45, 54]. To avoid excessive smoothing of heading

responses due to the slow temporal dynamics of calcium imaging, we deconvolved the calcium traces and inferred spikes for all analyses (Figure 1C). We then measured the response of each neuron as a function of the angular position of the cue card, revealing that a proportion of neurons in RSC faithfully represent heading (14.0%, 373/2665 neurons; Figure 1D-E), similar to the proportion found in freely moving rodents [6, 7]. However, we observed that mice did not always fully sample the entirety of the cage in each recording (Figure S1). Additionally, mice may have been able to use other sensory cues besides vision, such as odor, to determine their heading.

To isolate the visual contribution to heading representations, we transitioned to a controlled rotation design. We used guide bearings to limit translation while rotating the chamber with a motorized wheel (Figure 1F). This approach has three distinct advantages: 1) it creates a regular trial structure in the data, 2) it ensures equal sampling of the entire range of headings, and 3) it reduces changes in the appearance of the visual cues due to variable proximity during chamber translation. To take advantage of the trial structure of our data, we created a new method with a low false positivity rate to determine if a neuron was heading selective (Figure S2, see Methods). Using this method, we found a similar percentage heading neurons as in the experiments without controlled rotation, comprising 14.2% (452/3179 neurons) of the total number of cells recorded ($n = 16$ recordings over 5 mice, Figure 1G, Figure S3). We wanted to ensure that the recorded cells were not simply activated by the passing of the visual cue over a visual receptive field. We aligned all the cells using their cross-validated preferred direction (see Methods), showing that heading-responsive cells tile the entire circumference of the chamber, even when the cue card is outside of the visual field of the mouse; though we note there is overrepresentation of responses when the cue is centered in front of the mouse at 0°(Figure 1H). This suggests that the cells that we recorded are not simply relaying visual information. Next, we created a decoder to confirm that the population of recorded cells in a single recording contained sufficient information to accurately represent the heading of the animal. Briefly, the decoder uses the tuning curve of each neuron scaled by the activity at each time point to construct a population likelihood of perceived heading, and then selects the maximum likelihood as the predicted heading for that time point (Figure 1I). Using all of the heading cells in single recording, the decoder was able to predict the location of the cue card significantly above chance over multiple trials. ($t(8) = 5.4$, $p = 6.6 \times 10^{-4}$, paired t-test; Figure 1J). Together, these results suggest that the visual and proprioceptive input from the rotating chamber sufficiently drive dysgranular RSC neurons to accurately represent heading, even in the absence of vestibular modulation.

Heading cells exhibit similar preferred directions during rotation of the animal or the environment

Previous research has emphasized the importance of vestibular information for the function of the heading network [55], so we next investigated whether the same neurons exhibit matched tuning during head fixation in a rotating environment versus during rotation of the head in a fixed environment. To address this, we added a belt-driven rotation collar to the previous experimental set up, allowing physical rotation of the mouse head plate with the window centered underneath the imaging objective (Figure 2A). The rotation had a constant, low angular velocity to allow the animal to walk along as the head plate was rotated. This approach allowed us to compare responses in the same neurons across two conditions: 1) in which the head rotates but the chamber is fixed or 2) in which the chamber rotates while the head is fixed ($n = 5$ recordings across 4 mice; Figure 2B). Since the head is physically rotating under the microscope objective, we first registered each frame to a template calculated from the average frame during the chamber rotation recording (Figure 2C). After registration, we defined a single set of ROIs across the two recordings and manually checked the quality of each ROI for size, shape, and brightness to identify ROIs that contained the same cell across conditions (Figure 2D). We found that many neurons, though not all of them, exhibit similar tuning across the two conditions, with small differences in preferred direction ($V(32) = 14.1$, $p = 2.5 \times 10^{-4}$, V-test for nonuniformity against 0°; Figure 2E). Across all recordings, matched ROIs on average have the same heading preference with respect to wall pattern across conditions, suggesting that cells accurately represent heading with respect to the chamber's visual cues irrespective of head or chamber rotation (Figure 2F). Not all cells retain the same heading preference, possibly due to distal visual cues past the walls of the chamber, which are not informative in the chamber rotation condition, but provide potential landmarks in the head rotation condition.

Changing visual cues elicits coherent remapping in RSC neurons

The previous experiment demonstrates that many of the neurons we found that are tuned to changes in head angle are also tuned for changes in the rotation of the environment. Next, we wanted to confirm that heading-tuned neurons observed during head rotation exhibit similar population dynamics as HD cells. HD cells have been found to remap in different environments, while maintaining a constant angular offset between pairs of HD cells. As a consequence, moving an animal to an environment with new visual landmarks elicits "coherent remapping" [56], as the entire population rotates to align to the new landmarks, while retaining the same relative offsets between neurons (Figure 3A). To test whether heading cells in the rotating environment also have this quality, we replaced all of the visual cues on the chamber wall between recordings to alter the local landmarks and elicit remapping, creating two separate contexts. When comparing the same cells across the two contexts, we found that the majority of heading cells indeed shift by the same angular offset ($n = 12$ recordings over 4 mice; Figure 3B). The angular offset does is not consistent across different recordings because the remapping due to changing contexts is random. Therefore, to compare across recordings, we first calculated the "phase offset" of each neuron, defined as the difference in preferred heading across conditions. Then, iterating through each neuron, we subtracted each neuron's phase offset to the averaged phase offset of all other neurons in the same recording ("Δ phase offset"; see Methods) to determine whether the neuron coherently remapped along with the population. When combining measurements across all recordings, we found that changing contexts caused the population of heading cells to coherently remap, as indicated by low Δ phase offsets ($V(66) = 25.6$, $p = 4.9 \times 10^{-6}$, V-test for nonuniformity against $0°$; Figure 3C).

In summary, we show that heading cells retain their tuning whether vestibular signals are modulated (in head rotation) or not modulated (in chamber rotation). Additionally, we show that the heading network in a head-fixed preparation as a whole exhibits the same functional properties as in freely moving animals. Together, these results show that modulation of vestibular input is not necessary for eliciting heading responses if vision and proprioception are spared. Rather, many of the same heading neurons remain active and accurately represent the animal's heading relative to the moving environment. Importantly, these results also show that the mammalian heading network is capable of representing the animal's heading relative to the environment even when the head is immobilized.

The ADN and visual cortex send distinct information to RSC

In our previous experiments, we found that not all cells would retain their preferred direction across conditions or coherently remap, suggesting that there is significant heterogeneity in RSC, which may be due to differences in the inputs it receives from other brain regions. Previous anatomical tracing studies [36, 38] have shown that RSC receives direct projections from both ADN and the visual cortex which likely contribute to RSC heading representations. However, the responses of these projections in moving animals has not been studied, and the information that each area sends to RSC is not known. To measure the responses from RSC-projecting neurons in each of these regions, we microinjected an AAV expressing GCaMP7b into ADN or the higher visual areas anteromedial (AM)/posteromedial (PM) in separate cohorts of wild-type mice. We chose AM and PM since they provide the major input from visual cortex to RSC [57] as well as their role in the visual hierarchy [58]. We then imaged the axon terminals arising from ADN ($n = 17$ recordings over 4 mice) or AM/PM in RSC ($n = 7$ recordings over 3 mice; Figure 4A). In order to distinguish classical visual responses from heading responses, we used a pair of symmetric cues on opposite sides of the chamber so that an identical visual stimulus would pass in front of the mouse twice for each full chamber rotation. We also recorded in both light-on and light-off conditions to selectively gate visual input (Figure 4B). We postulated that projections carrying heading signals would exhibit unimodal peaks that persist in the light-off condition, accurately representing heading regardless of light condition or cue symmetry. On the other hand, projections communicating visual landmark signals would exhibit a light-sensitive and bimodal tuning curve, with peaks separated by approximately $180°$due to the symmetry of the visual stimulus (Figure 4C).

We found that responses from ADN and visual cortical projections exhibit distinct responses in these conditions. In the light-on condition, ADN axons show a unimodal tuning curve, whereas visual cortical axons show a bimodal tuning curve (Figure 4D, E). In the light-off condition, ADN axons maintain their response for several trials, whereas visual cortical axons lose their tuning. These results show that the information from the visual cortex is highly sensitive to environmental cues and cannot be entirely sufficient for driving heading responses, as any symmetrical environment would result in an inaccurate heading representation. The

accurate internal heading representation regardless of environmental symmetry suggests that the information from the visual cortex must be processed prior to being integrated into the heading network. Together, these results indicate that ADN and visual cortex send distinctively tuned projections to RSC, which provide a basis for aligning the heading signal with external cues.

A functional class of RSC neurons coregisters visual and heading signals

How do neurons in RSC combine the disparate responses from ADN and visual cortex? We imaged calcium activity in RSC cell bodies using the same experimental conditions, allowing us to determine whether RSC responses resemble thalamic or visual cortical inputs ($n = 36$ recordings over 6 mice). We found a diversity of responses in RSC that resembled both visual cortical inputs (discernible by a second peak in light) and ADN inputs (discernible by a single peak in the dark) (Figure 5A, Figure S4A-B). To help classify RSC responses, we fit a sum of Gaussians to the data then performed unsupervised clustering on the coefficients using a Gaussian mixture model (GMM) to separate the cells into functional classes (Figure 5B; see Methods). We found that the data were optimally clustered into three functional classes (see Methods), although we note that the responses span a continuum rather than fully isolated clusters.

The model returned a prominent class of cells that mirrored the tuning curves of ADN axons, with a unimodal peak that is stable in either light-on or light-off conditions, which we call "heading cells" (Figure 5C). We also found another class that mirrored the tuning curves of visual cortical axons, with a bimodal peak in the light-on condition that disappears in the light-off condition, which we call "landmark cells" (Figure 5D). Finally, the clustering returned a third major class of cells, which combined the responses of ADN and visual axons, exhibiting bimodal responses in the light-on condition, but changing to a more unimodal response profile in the light-off condition, which we call "alignment cells" (Figure 5E). The light-off peak in these alignment cells was always at the same location as one of the two peaks in the light-on condition, suggesting that landmark and heading responses are precisely coregistered in the alignment cells. Of the total number of tuned cells (13%), landmark cells made up the plurality of cells (35%), followed by alignment (28%), and heading cells (12%) (Figure 5F, Figure S4). We then compared the cell classes in measures of light sensitivity and bimodality (Figure 5G, H). Across the classes, landmark cells showed significantly greater sensitivity to light condition (mean RVL index = 0.83, 95% CI = [0.81, 0.84]) than either alignment (mean RVL index = 0.25, 95% CI = [0.20, 0.30]) or heading cells (mean RVL index = 0.17, 95% CI = [0.10, 0.24]). Although alignment and landmark cells differed in their light sensitivity, alignment and heading cells did not, suggesting that alignment cells are robust to changes in light, like heading cells. On a measure of bimodality, landmark cells exhibited the highest flip scores due to their dual peaks (mean flip score = 0.82, 95% CI = [0.74, 0.89]), being significantly greater than both alignment (mean flip score = 0.56, 95% CI = [0.49, 0.63]) and heading cells (mean flip score = 0.19, 95% CI = [0.10, 0.28]).

Since ADN and visual cortex send tuned projections to RSC, we hypothesized that the somatic responses would be a result of specific combinations of tuned connections. To show this, we computed an input index that compares each RSC neuron's response to the average response from ADN and visual cortical axons (Figure 5I). Comparing across clusters shows the responses of heading cells are most similar to ADN axons while landmark cells are most similar to visual cortical axons. Alignment cells have widely distributed input indices, suggesting that they may receive information from both sources, or from intra-RSC projections. These results support that projections from visual cortex and ADN synapse with specific targets in RSC, leading to a functional class of cells capable of coregistering visual cues and heading (Figure 5J).

Contributions of distinct classes to representation of heading

The functional classes observed would be expected to lead to very different representations of head direction. We sought to understand the contributions of each functional class to the population-level coding of heading. First, we confirmed that the heading network was able to accurately represent the animal's heading, even in an environment with symmetric visual information, by decoding heading from large populations of cells over 100 ms time bins. To combine multiple recordings, we created pseudopopulations of neurons by aligning trials across recordings (see Methods). In the light-on condition, the heading network shows remarkable accuracy in decoding heading, even in the presence of symmetric visual cues, although there is an over-representation of decoder errors clustered around 180°, a direct consequence of the contribution of landmark cells to heading

(mean fraction correct = 0.72, 95% CI = [0.66, 0.78], Figure 6A). When transitioning from light-on to light-off, there is a drop in the performance of the decoder, although the performance remains above chance, suggesting that the heading network continues to track heading, albeit less accurately, even in the absence of visual cues (mean fraction correct = 0.37, 95% CI = [0.31, 0.43], Figure 6A, bottom). In the transition from light-off to light-on, we found that the decoder rapidly recovered a high level of performance in the first trial following the transition (Figure 6B). Comparing decoder performance between the two transitions shows an interesting imbalance: light-on to light-off transitions show a gradual decline, whereas light-off to light-on transitions show a rapid recovery. These results confirm previous studies which have shown that the heading network gradually degrades in darkness, but is quickly restored in light [10, 25, 26].

To further parse the contributions of specific functional classes, we also performed population decoding restricted to cells of one response type (heading, landmark, alignment; Figure 5C-E). As with the entire pseudopopulation, we can examine the differences in decoder performance in light-on vs light-off conditions as well as the contribution of the symmetric visual cues, which manifests as increased 180°errors. We found that heading cells were able to accurately decode in both light-on (mean fraction correct = 0.41, 95% CI = [0.37, 0.44]) and light-off conditions (mean fraction correct = 0.27, 95% CI = [0.24, 0.30]), suggesting that they contribute to the heading signal in both conditions (Figure 6C). Because their decoder performance is lower than the population in the light-on condition, heading cells alone may be insufficient for providing an optimally representation of instantaneous heading. As expected based on their tuning curves, heading cells did not exhibit a preponderance of 180°errors (Figure S5), suggesting they do not represent visual information directly and were therefore not affected by the symmetric cues. In contrast, landmark cells have very high decoder performance in the light-on condition (mean fraction correct = 0.55, 95% CI = [0.46, 0.63]), with an over-representation of decoder errors at 180°(Figure S5), which immediately plummets to chance in the light-off condition (mean fraction correct = 0.14, 95% CI = [0.09, 0.18]; Figure 6D). This suggests that landmark cells strongly drive the heading signal when visual cues are present, but provide almost no contribution in their absence. Lastly, alignment cells show decoder performance that is between that of heading and landmark cells, taking advantage of improved decoding from the visual cues in the light-on condition (mean fraction correct = 0.43, 95% CI = [0.35, 0.50]), but retaining fairly accurate heading in the light-off condition (mean fraction correct = 0.34, 95% CI = [0.28, 0.40], Figure 6E). This suggests that alignment cells can take advantage of the visual cues in the light-on condition, while retaining accurate decoding in their absence in the light-off condition, positing that they may be responsible for integrating and registering visual landmark and heading information.

Taken together, we propose a working model to describe the distinct roles played by heading, landmark, and alignment cells in the registration of heading representations to visual cues (Figure 6F). First, in the light-on condition, all three classes are active, with landmark cells faithfully representing the position of the visual cues, heading cells relaying information from the heading network, and a subset of alignment cells coregistering both sources of information, resulting in a internal heading that is well aligned with the true external heading. (Figure 6F, left). In the light-off condition, the landmark cells are silenced, leaving the heading cells as the primary driver of internal heading, and the alignment class exhibiting a response matched to the heading cells (Figure 6F, center). Moreover, the lack of anchoring visual information causes the heading network to drift over time, leading to the internal heading to become offset from the true heading. Upon restoring visual cues in the light-on condition, landmark cells regain their tuning, relaying this information to the appropriate subset of alignment cells, which are in turn updated (Figure 6F, right). The alignment cells then update the heading cells, and the broader network via feedback projections from RSC to the ADN, updating the heading representation throughout the heading system. We propose that the co-registration of visual landmark and heading signals in the alignment cells thereby plays a critical role in aligning the heading representation to external visual cues.

Discussion

One of the key findings of this paper is that heading, the relative orientation of an animal in an environment, can be encoded separately from physical head direction in the heading network. This finding is consistent with previous studies in which humans solve complex virtual navigation tasks without the requirement of physical movement, suggesting that they can create an abstract mental map of their direction independent of physical

locomotion [59–62]. Research in invertebrates further supports this view, as the E-PG ("compass") neurons of the *Drosophila* central complex, an analog of the heading network, is active in virtual environments even when the fly is immobile [1, 29]. Here, we demonstrate that at least a subset of neurons in the mammalian heading network show a similar capability during head fixation, using multiple sensory inputs to accurately represent relative heading [33]. What benefits does the floating chamber design confer over traditional head-fixed virtual reality set ups? Besides providing a three-dimensional visual environment, the floating chamber maintains somatosensory and proprioceptive cues present during locomotion through a physical environment. Using a combination of these sensory cues, the heading cells (many of which would be classified as HD cells in freely moving conditions) appear to be able to compensate for the absence of vestibular information, although not all neurons maintained their tuning between head rotation and chamber rotation conditions. Because of the heterogeneity of responses in RSC, a subset of RSC heading cells may be more strongly driven by vestibular input, and therefore lose their response during head fixation; whereas other, more visually driven, neurons are still responsive. This is reminiscent of previous studies which found that including additional sensory modalities improves the coding of AHV [48, 63] and HD [33] cells. However, our results show that, even if there is reduced activity due to absence of vestibular input, neurons of the heading network in head-fixed mice remain functional and are able to accurately track heading, expanding the repertoire of experimental approaches.

The heading network has commonly been modeled as a ring attractor network, which encapsulates many of the observed properties of the heading signal [1, 64]. Within the core ring attractor, neurons represent heading via an "activity bump", which can be shifted around the ring by sensory inputs that represent rotational motion, including vestibular and visual inputs. Additionally, there are also sensory inputs which anchor the activity bump to external cues, such as visual landmarks. Recent work has begun to elucidate the specific cells and mechanisms that may be responsible for anchoring the ring attractor to visual landmarks. Many of these used similar approaches to ours, leveraging symmetric visual cues to segregate visually driven cells. Jacob et al., 2017 [43] found a specific class of cells that have bimodal tuning curves in a two-chamber symmetric environment, called "within-compartment bidirectional cells", that were postulated to develop their responses through Hebbian-based strengthening of visual information with information from the heading network. Similarly, LaChance et al., 2022 [65] found bidirectionally tuned cells in the postrhinal cortex that could represent and discriminate between symmetric visual cues, suggesting an important role in processing visual landmarks. However, there are some key differences in our findings. Previous work in RSC has found bimodal responses in two connected visually symmetric chambers, but not in a single chamber with symmetric cues [66]. In our recordings, we found cells in RSC with bimodal tuning curves in a single chamber with symmetric cues, akin to studies in postrhinal cortex [65]. We postulate that the difference in bimodal responses in RSC may be due to our experimental design, which fixes the mouse in the center, removing modulation of both the visual cues by chamber translation as well as vestibular signals. Moreover, recent work has suggested that visually evoked responses may be masked during active navigation [67]. We also find a novel class of alignment cells which encapsulate similar properties from previously described heading cell types in symmetrical environments, such as bimodal tuning curves [43, 65], uneven peak amplitudes [65], and persistent activity in darkness [43]. However, we are the first to report that these cells shift from bimodal tuning curves in light to aligned unimodal tuning curves in darkness, suggesting that they are capable of both encoding and registering both visual and heading signals.

Our results show that RSC integrates visual information into the heading network, but other areas in the HD may also play important roles. The postsubiculum shares many of the same properties as RSC, as it the only other area in the heading network which receives direct projections from both visual cortex and ADN [68, 69]. Lesioning postsubiculum degrades the heading signal in the ADN and results in an inability to register to visual landmarks, similar to RSC lesions [70]. Recent work has also suggested that the postrhinal cortex may also play a role, as it contains visually driven heading cells that can discriminate between symmetric landmarks [65]. Additionally, cells with bimodal responses have also been found in the medial entorhinal cortex [71], which has been show to affect RSC activity [72]. Given that cells in each of these areas exhibit similar visually-influenced tuning properties, are these systems redundant or complementary? Since the regions are highly interconnected [38, 73], it is possible that they may redundantly represent the same information, since registration of visual information is important for the heading network in spatial processing. Alternatively, the processing in each area may be complementary, biased by the strength of their connectivity with other brain regions [40]. Further studies will be needed to understand how the distributed

regions in the HD system interact during navigation.

In conclusion, our study provides evidence that neurons in the heading network are capable of representing the heading of the animal relative to the environment independent of physical head direction. The dysgranular RSC is able to combine multisensory information to create an abstracted map of heading, similar to how place cells can encode other variables besides position [20, 74, 75]. Finally, we propose a potential circuit based on a newly discovered class of neurons in RSC that act to coregister visual cues to the heading network. Future studies of how heading and other spatial signals are aligned to sensory input will be critical for understanding how internal representations of the spatial environment are generated, maintained, and updated by sensory information.

Methods

Animals

For cortex-wide calcium indicator expression, Emx1-Cre (Jax Stock #005628) × ROSA-LNL-tTA (Jax Stock #011008) × TITL-GCaMP6s (Jax Stock #024104) triple transgenic mice or Slc17a7-IRES2-Cre (Jax Stock #023527) × TITL2-GC6s-ICL-TTA2 (Jax Stock #031562) double transgenic mice were bred to express GCaMP6s in cortical excitatory neurons. For axon tracing experiments, wild-type C57BL/6J mice were used. For all imaging experiments, 6-12 week old mice of both sexes (12 males and 10 females) were implanted with a head plate and cranial window and imaged starting 2 weeks after recovery from surgical procedures and up to a maximum of 10 months after window implantation. The animals were housed on a 12h light/dark cycle in cages of up to 5 animals before the implants, and individually after the implants. All animal procedures were approved by the Institutional Animal Care and Use Committee at UC Santa Barbara.

Surgical Procedures

All surgeries were conducted under isoflurane anesthesia (3.5% induction, 1.5–2.5% maintenance). Prior to incision, the scalp was infiltrated with lidocaine (5 mg kg-1, subcutaneous) for analgesia and meloxicam (2 mg kg-1, subcutaneous) was administered pre-operatively to reduce inflammation. Once anesthetized, the scalp overlying the dorsal skull was sanitized and removed. The periosteum was removed with a scalpel and the skull was abraded with a drill burr to improve adhesion of dental acrylic. For all chamber-rotation mice, a 4 mm craniotomy was made centered over the midline (centered at 3.0 mm posterior to Bregma), leaving the dura intact. For a subset of these mice, Syn-GCaMP7b was injected into either AM (3.0mm anterior, 1.7mm lateral), PM (1.9mm anterior and 1.6mm lateral to Lambda), or ADN (0.8 mm posterior and 0.8mm lateral to Bregma, 3.2 mm depth [76]). For head rotation experiments, the 4 mm craniotomy was centered 3.0 mm posterior and 1.0 mm lateral to Bregma, so that the axis of rotation was not centered over the sagittal sinus. A cranial window was implanted over the craniotomy and sealed first with silicon elastomer (Kwik-Sil, World Precision Instruments) then with dental acrylic (C&B-Metabond, Parkell) mixed with black ink to reduce light transmission. The cranial windows were made of two rounded pieces of coverglass (Warner Instruments) bonded with a UV-cured optical adhesive (Norland, NOA61). The bottom coverglass (4 mm) fit tightly inside the craniotomy while the top coverglass (5 mm) was bonded to the skull using dental acrylic. A custom-designed stainless-steel head plate (eMachineShop) was then affixed using dental acrylic. In all conditions, the head plate was carefully positioned to ensure a natural gait under recording conditions. After surgery, mice were administered carprofen (5 mg kg^{-1}, oral) every 24h for 3 days to reduce inflammation. The full specifications and designs for head plate and head fixation hardware can be found on our institutional lab website (`https://goard.mcdb.ucsb.edu/resources`).

Floating chamber design and set up

For the floating chamber experiments (Figure 1A), we used a set up based on the Mobile HomeCage system (Neurotar Ltd.). Briefly, a 250 mm diameter carbon fiber chamber was placed on top of a perforated metal base. Pressurized air fed into the metal base floated the chamber, reducing friction and allowing the chamber to move readily. Mice were then head fixed in the center of this chamber and allowed to ambulate, which

moved the chamber around the mouse while the mouse remained still. The air pressure was tuned (2-4 PSI) so that the chamber provided enough friction to create a natural gait. The chamber contains a set of magnets which are read by the base in order to report information about the position of the chamber (Tracking Software v2.2.1, Neurotar Ltd.), which are then transformed using custom code (MATLAB 2020b, Mathworks) to extract the position, angle and velocity of the mouse relative to the chamber.

For single cue experiments, the walls of the chamber contained a single black cue (width: 60mm) set on top of a white noise background that spanned the entire inner circumference of the chamber.

For dual cue experiments, the walls of the chamber contained a repeating pattern of stars or bars (width: 180mm), in an A - B - A - B pattern. These stimuli were separated by black bars to separate the cues (width: 15mm).

For remapping experiments, the walls of the chamber was divided into four quadrants, each with a different stimulus. Between recordings, the stimuli were replaced with four new unique stimuli in complete darkness, so that the mouse could not see the transition between stimuli.

All wall cues were printed on nylon waterproof paper and attached to the chamber walls using double-sided tape.

Forced rotation experiments

To ensure even sampling of the entire rotation space, we carefully controlled the rotation of the chamber. Three stabilizing bearings (608-2RS) were mounted on optical posts (TR-series, Thorlabs) and placed around the cage to eliminate any X-Y translation. A DC motor (ZGA37RG, Greartisan) was coupled to a rubber wheel and used to spin the chamber using the outer surface. The speed of the DC motor was controlled with a microcontroller (UNO R3, Arduino) drive the rotation of the chamber (3-7 rpm).

The chamber was rotated for 90 - 120s followed by a 5s rest period, which was then repeated 2 - 6 times for each recording. Mice were monitored via video to ensure that they followed along with the chamber rotation. The total time spent rotating on the floating air chamber never exceeded 15 minutes, in order to limit potential discomfort.

For experiments in light and darkness, the lights in the experimental box were switched using a micro-controller (UNO R3, Arduino). The initial repeat was always performed in a light on trial, so that the mouse could register visual landmarks in its environment. Afterwards, the box lights were turned on or off in between repeats, during the rest period.

The chamber was thoroughly cleaned and disinfected between experiments in order to remove any odor traces.

Physical head rotation experiments

The head rotation apparatus consisted of a rotation collar (LCRM2, Thorlabs Inc.) attached to a translating mount (LM2XY, Thorlabs Inc.) and a quick release adapter (SM2QA, Thorlabs Inc.) The translating mount allowed for inependent adjustment of the imaging field about the axis of rotation to optimize the imaging field. The quick release adapter was used in order to easily head fix mice to the apparatus. A closed timing belt for 3D printers (2GT-610) was looped around the rotation collar and attached to a DC motor (ZGHA37RG, Greartisan) and belt tensioner (6mm belt pulley). Due to the danger of physically rotating the mouse, we limited the speed of the head rotation to 2 rpm and installed safety bars alongside the body of the mouse to ensure that the body of the mouse did not become twisted under the collar.

Two-photon imaging

After >2 weeks recovery from surgery, GCaMP6s fluorescence was imaged using a Bruker Investigator two-photon microscopy system with a resonant galvo-scanning module. Posterior dysgranular RSC was targeted by imaging just lateral of the sagittal sinus and just anterior the the transverse sinus.

For fluorescence excitation, we used a Ti:Sapphire laser (Mai-Tai eHP, Newport) with dispersion compensation (DeepSee, Newport) tuned to $\lambda = 920nm$. For collection, we used GaAsP photomultiplier tubes (Hamamatsu). To achieve a wide field of view, we used a 16×0.8 NA microscope objective (Nikon) and imaged at a $414 \times 414\mu m$, $690 \times 690\mu m$, or $829 \times 829\mu m$ field of view spanning 760×760 pixels. Laser power ranged from 40 to 75mW at the sample depending on GCaMP6s expression levels. Photobleaching

was minimal ($< 1\%$ min^{-1}) for all laser powers used. A custom stainless-steel light blocker (eMachineShop) was mounted to the head plate and interlocked with a tube around the objective to prevent ambient light from reaching the PMTs.

Two-photon post-processing

Images were acquired using PrairieView acquisition software (Bruker) and converted into TIF files. All subsequent analyses were performed in MATLAB (Mathworks) using custom code (`https://github.com/ucsb-goard-lab/Two-photon-calcium-post-processing`). First, images were corrected for X-Y movement by registration to a reference image (the pixel-wise mean of all frames) using 2-dimensional cross correlation.

To identify responsive neural somata, a pixel-wise activity map was calculated using a modified kurtosis measure. Neuron cell bodies were identified using local adaptive threshold and iterative segmentation. Automatically defined ROIs were then manually checked for proper segmentation in a graphical user interface (allowing comparison to raw fluorescence and activity map images). To ensure that the response of individual neurons was not due to local neuropil contamination of somatic signals, a corrected fluorescence measure was estimated according to:

$$F_{\text{corrected}}(n) = F_{\text{soma}}(n) - \alpha(F_{\text{neuropil}}(n) - \overline{F}_{\text{neuropil}}) \tag{1}$$

where F_{neuropil} was defined as the fluorescence in the region $< 30\mu m$ from the ROI border (excluding other ROIs) for frame n. $\overline{F}_{\text{neuropil}}$ is $F_{neuropil}$ averaged over all frames. α was chosen from [01] to minimize the Pearson's correlation coefficient between $F_{\text{corrected}}$ and F_{neuropil}. The $\Delta F/F$ for each neuron was then calculated as:

$$\Delta F/F = (F_{\text{n}} - F_0)/F_0 \tag{2}$$

where F_n is the corrected fluorescence ($F_{corrected}$) for frame n and F_0 defined as the mode of the corrected fluorescence density distribution across the entire time series.

De-rotation of image time series

Because the microscope is fixed relative to the mouse in the head rotation experiments, the images from the microscope were de-rotated in order to be properly processed [77]. The initial non-rotation period was used to create a template that the remainder of the images would be registered to. Registration was performed by maximizing the Mattes mutual information between each frame and the template via a one plus one optimizer (MATLAB, Mathworks). The geometric transformation of the previous successfully registered image was applied as an initial transform in order to optimize the performance and speed of the registration. After de-rotating each frame, an occupancy map was calculated from the resulting images, and the image was cropped so that only areas that contained all frames were included in further analyses. The final image series was subsequently analyzed using the two-photon processing pipeline described above. All the associated code for derotation can be found here: *(url to final version to be posted upon acceptance)*

Axon terminal imaging

For axon terminal imaging, we processed the TIF files using the Python implementation of Suite2P [78]. Briefly, TIFs underwent rigid registration using regularized phase correlations. Regions of interest were extracted via clustering correlated pixels, and were manually checked based on location, morphology, and $\Delta F/F$ activity. A specific configuration of Suite2P was used that is optimized for detecting axon processes [79]. After defining ROIs, we used custom code (MATLAB) to check that the same axon process was not sampled multiple times (for ROIs with Pearson correlation > 0.5, one ROI was excluded).

Analysis of calcium data

To avoid low pass filtering of heading tuning curves due to slow calcium dynamics, we used a MATLAB implementation of a sparse, nonnegative convolution algorithm (OASIS) on $\Delta F/F$ traces [80] with an autoregressive model of order 1 for the convolution kernel.

For the floating chamber experiments with voluntary control, the Rayleigh vector length (RVL) was used to determine if a cell was heading selective. The RVL was calculated for each cell and compared against a shuffled distribution. To create the shuffled distribution, each cell's spike data was circularly shuffled and the tuning curve and resulting RVL was calculated. This was repeated 1000 times to create a distribution of shuffled RVLs. Cells whose true RVL met or exceeded the 99th percentile of this distribution were considered to be heading selective.

For calculation of heading selectivity in the rotating chamber experiments, each cell's spike time series was divided into trials, with each trial representing a single full rotation of the chamber. To calculate tuning curves, the orientation of the chamber at each frame was first binned into 60 bins of 6 degrees. Then, the response was calculated for each trial using the spike rate of the cell at each heading bin, smoothed by a 15°moving average filter. The overall tuning curve was calculated by averaging the responses across all trials.

Next, we determined whether each cell (or axon terminal) was significantly heading selective. First, the reliability each cell's heading preference across trials was calculated by randomly splitting the trials into two groups and calculating the correlation coefficient between the resulting tuning curves. Then, each trial's activity was circularly shifted prior to calculating the correlation coefficient. This was repeated 1000 times for each cell, creating a real and shuffled distribution, which was compared via a two-sample Kolmogorov-Smirnov test.

Cohen's d was calculated to gauge the separation between the two distributions. A cell was considered reliable if it passed the two-sample Kolmogorov-Smirnov test at $p < 0.1$ and had a Cohen's $d > 0.8$. Additionally, A single-term (for single cue) or two-term (for dual cue) gaussian was fit to the trial averaged tuning curve as well as the trial averaged shuffled tuning curves. As before, the tuning curves were shuffled and fit 1000 times. The goodness of fit (r^2) of the true fit was compared against the 90th percentile of r^2 for the shuffled fits to determine if the cell's tuning curve had the proper shape. These threshold values were chosen so that the combined significance value of the two measures is $p = 0.01$. When repeating these procedures using pre-shuffled data, no cells passed these criteria, suggesting that the number of heading selective cells is accurate, and not due to chance.

To compare tuning curves across cells regardless of preferred direction, a cross-validated alignment was performed. For each trial, the responses from every other trial was used to construct a tuning curve, and the peak index of that tuning curve was used to align the held out trial. For light-on and light-off experiments, individual tuning curves for each condition were first calculated by only averaging trials that belonged to each light condition. Cross-validated alignment was performed on the light-on tuning curves, and the offsets applied to the light-off tuning curves, so that the same circular offset was applied to both conditions.

Calculation of coherent remapping

To determine whether or not a population of neurons remapped coherently, a cross-validated procedure was created. For each neuron in a recording, the difference between its preferred direction in the first and second context was calculated. Next, all other cells in the recording were used to calculate an "expected offset" by taking the median across all cell pair differences in preferred direction across contexts. Lastly, the difference between the neuron of interest and the median difference was taken to determine if the neuron of interest remapped coherently with the remainder of the population. This procedure can be summarized as follows:

$$\Delta\text{phase offset}_n = (\text{pref}_{(A,\,n)} - \text{pref}_{(B,\,n)}) - (\widetilde{\text{pref}}_{(A,\,[0,\,N]\neq n)} - \widetilde{\text{pref}}_{(B,\,[0,\,N]\neq n)}) \tag{3}$$

where pref_A and pref_B is the preferred direction in context A or B, respectively, of neuron n and N is the total number of neurons. $\widetilde{\text{pref}}$ denotes the median of preferred directions. Perfect remapping would result in a difference of 0, suggesting that the neuron remapped the exact same amount as the population. This process was repeated for each recording to measure the amount of coherent remapping for each neuron in each recording. These values were compared against a shuffled distribution, in which random neurons were chosen and compared, rather than defined cell pairs.

Clustering of RSC soma responses

To categorize the response profiles of RSC somata, unsupervised clustering was performed. First, all cells were fit with a sum of Gaussians as defined below for both light-on and light-off conditions:

$$f(x) = a_0 + a_1 \times e^{-((x-b_1)/c_1)^2} + a_2 \times e^{-((x-b_2)/c_2)^2} \tag{4}$$

where a_0 is the baseline offset, a_1, b_1, c_1, a_2, b_2, and c_2 are the amplitude, location, and standard deviation for the first and second peaks, respectively. The coefficients a_1, a_2, c_1 and c_2 for each the light-on and light-off tuning curves were fit with an 8 component Gaussian mixture model (GMM). Coefficients b_1 and b_2 were omitted so that the location of the peak was not a determining factor in clustering. A cluster evaluation using silhouette analysis was performed to determine the optimal number of clusters, which reported a local maximum at $k = 3$ clusters, resulting in a 3 component GMM. Following clustering by the GMM, an additional exclusion step was performed to remove cells with poor tuning curves. The archetypal cluster response was created by averaging all the tuning curves within a single cluster, and the correlation coefficient between each member and the archetypal response was calculated. Individual cells with a correlation < 0.5 were moved to an unclassified cluster.

Because of the high dimensionality of the GMM components, a dimensionality reduction was performed for visualization (Figure 4B). First, the GMM was used to generate 100,000 data points from the three defined components. An LDA was trained on these data points, and the weights from the trained model were used to reduced the dimensionality of the real data to the first two dimensions for visualization.

Calculation of light sensitivity

Light sensitivity was calculated as an index based on the Rayleigh vector length (RVL) of each tuning curve. Because the RVL considers both direction and magnitude, we first used an angle doubling procedure to turn bimodal distributions into unimodal distributions, similar to previous work. The glsrvl index was then calculated for the light-on and light-off tuning curves as follows:

$$RVL_{\text{index}} = (RVL_{\text{ON}} - RVL_{\text{OFF}})/(RVL_{\text{ON}} + RVL_{\text{OFF}}) \tag{5}$$

where RVL_{ON} is the cell's RVL in light-on and RVL_{OFF} is the cell's RVL in light-off. This index ranges from $[-1, 1]$, with values closer to -1 indicaitng stronger tuning in light-off, value closer to 1 indicating stronger tuning in light-on, and values around 0 indicating equal strength tuning in both conditions.

Calculation of bimodality

To represent the bimodality of a neuron, we used a flip score metric also described previously. Briefly, an autocorrelation of each cell's tuning curve was performed. A bimodal cell resulted in a peak centered at 180°, which was absent in unimodal cells. The flip score was then calculated as follows:

$$\text{Flip Score} = CC_{180^\circ} - (CC_{90^\circ} + CC_{270^\circ})/2 \tag{6}$$

where CC_{180°, CC_{90°, and CC_{270° are the correlation coefficients of the autocorrelation at the 180°, 90°, and 270°positions, respectively.

Calculation of input index

An input index was calculated to determine the degree of similarity between each RSC soma's tuning curve and ADN or visual axonal responses. First a two-term Gaussian was fit to tuning curves from the ADN or visual cortical axonal responses, similar to for clustering rsc soma. Then a Gaussian mixture model was independently fit to each of the datasets, so that there was a single GMM for the ADN axonal data and another for the visual cortical axonal data. Next, the Mahalanobis distance was calculated for each rsc soma to eachGMM. Finally, the input index was calculated as follows:

$$\text{Input Index} = (D_{\text{VIS}} + D_{\text{ADN}})/(D_{\text{VIS}} + D_{\text{ADN}}) \tag{7}$$

where D_{ADN} is the Mahalanobis distance between each cell and the center of the GMM fit to the ADN axon data, and D_{VIS} is the same, but for the visual cortical axon data. Scores closer to -1 indicate that the cell has tuning more similar to ADN and scores closer to 1 indicate that the cell has tuning more similar to visual cortical projections.

Decoding RSC somatic activity

Preprocessing and alignment of calcium data

In order to aggregate trial data across all recordings, the follow preprocessing steps were performed. First, each rest period in which the chamber does not rotate between light-on and light-off conditions was identified. Individual trials were then defined as full rotations either preceding or following the rest period, so that each trial contained a full rotation of the chamber. For light-off to light-on conditions, the rest period was identified that separated light-off from light-on periods. By defining full trials about the rest period, each trial was ensured to fully span 360°. Next, minor variations in the speed of rotation between individual trials were accounted for by resampling both the heading information and neural data to be equal length (200 bins) across all trials in all recordings. Last, to ensure that the training data were not used for decoding, we calculated each cell's tuning curve on a trial by trial basis, including all data except those associated with that trial. Therefore, each trial had an associated tuning curve constructed of that cell's response in all trials except the one currently being decoded.

For single recording decoding (Figure 1J), recordings with fewer than 10 heading cells were excluded.

Decoding strategy

After preprocessing, the data were aggregated and used to decode heading on a trial by trial basis [81]. First, a population-level likelihood curve was constructed as follows:

$$\text{likelihood}_t = (F\vec{R}_t \times T) \oslash \sum (F\vec{R}_t \times T) \tag{8}$$

where $F\vec{R}_t$ is a vector of firing rates of all neurons at time t, T is a matrix containing the tuning weights of all neurons, and $\oslash$ represents element-wise division. The index of the maximum likelihood of the curve was used to determine the decoded heading bin at each time point.

Calculating decoder performance metrics

Because each pseudopopulation had uneven numbers of neurons, we first performed a bootstrapping procedure prior to calculating performance metrics. We sampled, without replacement, 180 neurons from each group and performed the following analyses on these subpopulations, then repeated the process 5000 times. The average percent correct was calculated for each bootstrapped sample and the 2.5^{th} and 97.5^{th} percentile were taken to contrsuct the 95%CI. If the confidence interval did not include chance (0.18), the percent correct was deemed to be statistically significant.

The decoder error for each frame was calculated as follows:

$$\text{Decoder Error} = |H_{\mathrm{decoded}} - H_{\mathrm{actual}}| \tag{9}$$

where H_{decoded} is the decoded heading at each frame and H_{actual} is the actual heading at each frame. Because of the overrepresentation of 180°errors due to the landmark cell contribution, we found that the average decoder error did not well represent the actual trial performance. Therefore, in addition to decoder error, we calculated the percent correct for each trial as follows:

$$\text{Percent Correct} = \sum (\text{Decoder Error} < 18^\circ)/N_{\mathrm{frames}} \times 100 \tag{10}$$

where N_{frames} is the total number of frames in the current trial.

Statistical Information

To test decoding error across recordings, paired t-tests were performed. To test whether angular data were clustered around a mean angle, a V-test was performed (Circular Statistics Toolbox, MATLAB). For all other significance testing, bootstrapped 95% confidence intervals were calculated. The confidence interval were then compared against either other confidence intervals or reference numbers. If there was no overlap between the confidence interval and the reference, it was considered to be statistically significant. When performing bootstrapping, data were randomly sampled with replacement. All statistical tests were performed as two-tailed tests.

Code Availability

All of the code for generating Figures 1-6 is available on the following GitHub repository: *(url to final version to be posted upon acceptance)*

Data Availability

All of the processed imaging data used for making Figures 1-6 is available in the following repository: *(url to final version to be posted upon acceptance)*

Contributions

K.K.S. and M.J.G. designed the experiments and analyses. K.K.S. conducted the experiments and analyzed the data. K.K.S. and M.J.G. wrote the paper.

Acknowledgements

We would like to thank Pierre-Yves Jacob, Kate Jeffery, Sung Soo Kim, Patrick LaChance, Cris Niell, Jeffrey Taube, and Ningyu Zhang for discussion of the manuscript. This work was supported by grants to M.J.G. from NIH (R01 NS121919), NSF (1707287), the Whitehall Foundation, and the Larry L. Hillblom Foundation.

References

1. Kim, S. S., Rouault, H., Druckmann, S. & Jayaraman, V. Ring attractor dynamics in the Drosophila central brain. *Science* **356,** 849–853 (2017).
2. Seelig, J. D. & Jayaraman, V. Neural dynamics for landmark orientation and angular path integration. *Nature* **521,** 186–191 (2015).
3. Beetz, M. J. *et al.* Flight-induced compass representation in the monarch butterfly heading network. *Current Biology* **32,** 338–349.e5 (2022).
4. Taube, J. S. Head direction cells recorded in the anterior thalamic nuclei of freely moving rats. *Journal of Neuroscience* **15,** 70–86 (1995).
5. Leutgeb, S., Ragozzino, K. E. & Mizumori, S. J. Convergence of head direction and place information in the CA1 region of hippocampus. *Neuroscience* **100,** 11–19 (2000).
6. Cho, J. & Sharp, P. E. Head direction, place, and movement correlates for cells in the rat retrosplenial cortex. *Behavioral Neuroscience* **115,** 3–25 (2001).
7. Chen, L. L., Lin, L. H., Green, E. J., Barnes, C. A. & McNaughton, B. L. Head-direction cells in the rat posterior cortex - I. anatomical distribution and behavioral modulation. *Experimental Brain Research* **101,** 8–23 (1994).
8. Stackman, R. W. & Taube, J. S. Firing properties of rat lateral mammillary single units: Head direction, head pitch, and angular head velocity. *Journal of Neuroscience* **18,** 9020–9037 (1998).

9. Taube, J. S., Muller, R. U. & Ranck, J. B. Head-direction cells recorded from the postsubiculum in freely moving rats. I. Description and quantitative analysis. *Journal of Neuroscience* **10,** 420–435 (1990).

10. Taube, J. S., Muller, R. U. & Ranck, J. B. Head-direction cells recorded from the postsubiculum in freely moving rats. II. Effects of environmental manipulations. *Journal of Neuroscience* **10,** 436–447 (1990).

11. Knierim, J. J., Kudrimoti, H. S. & McNaughton, B. L. Place cells, head direction cells, and the learning of landmark stability. *Journal of Neuroscience* **15,** 1648–1659 (1995).

12. Blair, H. T. & Sharp, P. E. Anticipatory head direction signals in anterior thalamus: Evidence for a thalamocortical circuit that integrates angular head motion to compute head direction. *Journal of Neuroscience* **15,** 6260–6270 (1995).

13. Taube, J. S. & Muller, R. U. Comparisons of head direction cell activity in the postsubiculum and anterior thalamus of freely moving rats. *Hippocampus* **8,** 87–108 (1998).

14. Taube, J. S. & Bassett, J. P. Persistent Neural Activity in Head Direction Cells. *Cerebral Cortex* **13,** 1162–1172 (2003).

15. Stackman, R. W. & Taube, J. S. Firing properties of head direction cells in the rat anterior thalamic nucleus: Dependence on vestibular input. *Journal of Neuroscience* **17,** 4349–4358 (1997).

16. Stackman, R. W., Clark, A. S. & Taube, J. S. Hippocampal spatial representations require vestibular input. *Hippocampus* **12,** 291–303 (2002).

17. Muir, G. M. *et al.* Disruption of the head direction cell signal after occlusion of the semicircular canals in the freely moving chinchilla. *Journal of Neuroscience* **29,** 14521–14533 (2009).

18. Blair, H. T., Cho, J. & Sharp, P. E. Role of the lateral mammillary nucleus in the rat head direction circuit: A combined single unit recording and lesion study. *Neuron* **21,** 1387–1397 (1998).

19. Frohardt, R. J., Bassett, J. P. & Taube, J. S. Path integration and lesions within the head direction cell circuit: Comparison between the roles of the anterodorsal thalamus and dorsal tegmental nucleus. *Behavioral Neuroscience* **120,** 135–149 (2006).

20. Aronov, D., Nevers, R. & Tank, D. W. Mapping of a non-spatial dimension by the hippocampal-entorhinal circuit. *Nature* **543,** 719–722 (2017).

21. Arleo, A. *et al.* Optic flow stimuli update anterodorsal thalamus head direction neuronal activity in rats. *Journal of Neuroscience* **33,** 16790–16795 (2013).

22. Zugaro, M. B., Berthoz, A. & Wiener, S. I. Background, but not foreground, spatial cues are taken as references for head direction responses by rat anterodorsal thalamus neurons. *The Journal of neuroscience : the official journal of the Society for Neuroscience* **21** (2001).

23. Bassett, J. P. *et al.* Passive movements of the head do not abolish anticipatory firing properties of head direction cells. *Journal of Neurophysiology* **93,** 1304–1316 (2005).

24. Shinder, M. E. & Taube, J. S. Active and passive movement are encoded equally by head direction cells in the anterodorsal thalamus. *Journal of Neurophysiology* **106,** 788–800 (2011).

25. Goodridge, J. P., Dudchenko, P. A., Worboys, K. A., Golob, E. J. & Taube, J. S. Cue control and head direction cells. *Behavioral Neuroscience* **112,** 749–761 (1998).

26. Zugaro, M. B., Arleo, A., Berthoz, A. & Wiener, S. I. Rapid spatial reorientation and head direction cells. *Journal of Neuroscience* **23,** 3478–3482 (2003).

27. Wallace, D. G., Hines, D. J., Pellis, S. M. & Whishaw, I. Q. Vestibular information is required for dead reckoning in the rat. *Journal of Neuroscience* **22,** 10009–10017 (2002).

28. Zheng, Y., Goddard, M., Darlington, C. L. & Smith, P. F. Long-Term deficits on a foraging task after bilateral vestibular deafferentation in rats. *Hippocampus* **19,** 480–486 (2009).

29. Kim, S. S., Hermundstad, A. M., Romani, S., Abbott, L. F. & Jayaraman, V. Generation of stable heading representations in diverse visual scenes. *Nature* **576,** 126–131 (2019).

30. Royden, C. S., Banks, M. S. & Crowell, J. A. The perception of heading during eye movements. *Nature* **360,** 583–585 (1992).

31. Pettorossi, V. E. & Schieppati, M. Neck Proprioception Shapes Body Orientation and Perception of Motion. *Frontiers in Human Neuroscience* **8,** 895 (2014).

32. Gasbarri, A., Packard, M. G., Campana, E. & Pacitti, C. Anterograde and retrograde tracing of projections from the ventral tegmental area to the hippocampal formation in the rat. *Brain Research Bulletin* **33,** 445–452 (1994).

33. Asumbisa, K., Peyrache, A. & Trenholm, S. Flexible cue anchoring strategies enable stable head direction coding in both sighted and blind animals. *bioRxiv,* 2022.01.12.476111 (2022).

34. Vann, S. D. & Aggleton, J. P. Selective dysgranular retrosplenial cortex lesions in rats disrupt allocentric performance of the radial-arm maze task. *Behavioral Neuroscience* **119,** 1682–1686 (2005).

35. Clark, B. J., Bassett, J. P., Wang, S. S. & Taube, J. S. Impaired head direction cell representation in the anterodorsal thalamus after lesions of the retrosplenial cortex. *Journal of Neuroscience* **30,** 5289–5302 (2010).

36. Van Groen, T. & Michael Wyss, J. Connections of the retrosplenial granular a cortex in the rat. *Journal of Comparative Neurology* **300,** 593–606 (1990).

37. Van Groen, T. & Wyss, J. M. Connections of the retrosplenial granular b cortex in the rat. *Journal of Comparative Neurology* **463,** 249–263 (2003).

38. Van Groen, T. & Wyss, J. M. Connections of the retrosplenial dysgranular cortex in the rat. *Journal of Comparative Neurology* **315,** 200–216 (1992).

39. Shibata, H. Efferent projections from the anterior thalamic nuclei to the cingulate cortex in the rat. *Journal of Comparative Neurology* **330,** 533–542 (1993).

40. Fischer, L. F., Soto-Albors, R. M., Buck, F. & Harnett, M. T. Representation of visual landmarks in retrosplenial cortex. *eLife* **9** (2020).

41. Alexander, A. S. & Nitz, D. A. Retrosplenial cortex maps the conjunction of internal and external spaces. *Nature Neuroscience* **18,** 1143–1151 (2015).

42. Page, H. J. & Jeffery, K. J. Landmark-based updating of the head direction system by retrosplenial cortex: A computational model. *Frontiers in Cellular Neuroscience* **12,** 191 (2018).

43. Jacob, P. Y. *et al.* An independent, landmark-dominated head-direction signal in dysgranular retrosplenial cortex. *Nature Neuroscience* **20,** 173–175 (2017).

44. Auger, S. D., Mullally, S. L. & Maguire, E. A. Retrosplenial cortex codes for permanent landmarks. *PLoS ONE* **7,** e43620 (2012).

45. Franco, L. M. & Goard, M. J. A distributed circuit for associating environmental context with motor choice in retrosplenial cortex. *Science Advances* **7** (2021).

46. Cooper, B. G. & Mizumori, S. J. Retrosplenial cortex inactivation selectivity impairs navigation in darkness. *NeuroReport* **10,** 625–630 (1999).

47. Whishaw, I. Q., Maaswinkel, H., Gonzalez, C. L. & Kolb, B. Deficits in allothetic and idiothetic spatial behavior in rats with posterior cingulate cortex lesions. *Behavioural Brain Research* **118,** 67–76 (2001).

48. Keshavarzi, S. *et al.* Multisensory coding of angular head velocity in the retrosplenial cortex. *Neuron* **110,** 532–543.e9 (2022).

49. Zhang, N., Grieves, R. M. & Jeffery, K. J. Title: Environment symmetry drives a multidirectional code in rat retrosplenial cortex 1 (0009).

50. Harvey, C. D., Coen, P. & Tank, D. W. Choice-specific sequences in parietal cortex during a virtual-navigation decision task. *Nature* **484,** 62–68 (2012).

51. Saleem, A. B., Diamanti, E. M., Fournier, J., Harris, K. D. & Carandini, M. Coherent encoding of subjective spatial position in visual cortex and hippocampus. *Nature* **562,** 124–127 (2018).

52. Sofroniew, N. J., Cohen, J. D., Lee, A. K. & Svoboda, K. Natural whisker-guided behavior by head-fixed mice in tactile virtual reality. *Journal of Neuroscience* **34,** 9537–9550 (2014).

53. Kislin, M. *et al.* Flat-floored air-lifted platform: A new method for combining behavior with microscopy or electrophysiology on awake freely moving rodents. *Journal of Visualized Experiments,* e51869 (2014).

54. Powell, A. *et al.* Stable Encoding of Visual Cues in the Mouse Retrosplenial Cortex. *Cerebral Cortex* **30,** 4424–4437 (2020).

55. Yoder, R. M. & Taube, J. S. The vestibular contribution to the head direction signal and navigation. *Frontiers in Integrative Neuroscience* **8,** 32 (2014).

56. Yoganarasimha, D., Yu, X. & Knierim, J. J. Head direction cell representations maintain internal coherence during conflicting proximal and distal cue rotations: Comparison with hippocampal place cells. *Journal of Neuroscience* **26,** 622–631 (2006).

57. Wang, Q., Sporns, O. & Burkhalter, A. Network analysis of corticocortical connections reveals ventral and dorsal processing streams in mouse visual cortex. *Journal of Neuroscience* **32,** 4386–4399 (2012).

58. Sit, K. K. & Goard, M. J. Distributed and retinotopically asymmetric processing of coherent motion in mouse visual cortex. *Nature Communications* **11,** 1–14 (2020).

59. Maguire, E. A., Burgess, N. & O'Keefe, J. Human spatial navigation: Cognitive maps, sexual dimorphism, and neural substrates. *Current Opinion in Neurobiology* **9,** 171–177 (1999).

60. Ekstrom, A. D. *et al.* Cellular networks underlying human spatial navigation. *Nature* **425,** 184–187 (2003).

61. Wolbers, T. & Büchel, C. Dissociable retrosplenial and hippocampal contributions to successful formation of survey representations. *Journal of Neuroscience* **25,** 3333–3340 (2005).

62. Yu, S. *et al.* Age-Related Changes in Spatial Navigation Are Evident by Midlife and Differ by Sex. *Psychological Science* **32,** 692–704 (2021).

63. Blair, H. T. & Sharp, P. E. Visual and vestibular influences on head-direction cells in the anterior thalamus of the rat. *Behavioral Neuroscience* **110,** 643–660 (1996).

64. Skaggs, W. E., Knierim, J. J., Kudrimoti, H. S. & McNaughton, B. L. A model of the neural basis of the rat's sense of direction. *Advances in neural information processing systems* **7,** 173–180 (1995).

65. LaChance, P. A., Graham, J., Shapiro, B. L., Morris, A. J. & Taube, J. S. Landmark-modulated directional coding in postrhinal cortex. *Science Advances* **8,** 8404 (2022).

66. Lozano, Y. R. *et al.* Retrosplenial and postsubicular head direction cells compared during visual landmark discrimination. *Brain and Neuroscience Advances* **1,** 239821281772185 (2017).

67. Purandare, C. S. *et al.* Moving bar of light evokes vectorial spatial selectivity in the immobile rat hippocampus. *Nature* **602,** 461–467 (2022).

68. Taube, J. S. The head direction signal: Origins and sensory-motor integration. *Annual Review of Neuroscience* **30,** 181–207 (2007).

69. Angelaki, D. E. & Laurens, J. The head direction cell network: attractor dynamics, integration within the navigation system, and three-dimensional properties. *Current Opinion in Neurobiology* **60,** 136–144 (2020).

70. Goodridge, J. P. & Taube, J. S. Interaction between the postsubiculum and anterior thalamus in the generation of head direction cell activity. *Journal of Neuroscience* **17,** 9315–9330 (1997).

71. Kornienko, O., Latuske, P., Bassler, M., Kohler, L. & Allen, K. Non-rhythmic head-direction cells in the parahippocampal region are not constrained by attractor network dynamics. *eLife* **7** (2018).

72. Van Wijngaarden, J. B., Babl, S. S. & Ito, H. T. Entorhinal-retrosplenial circuits for allocentric-egocentric transformation of boundary coding. *eLife* **9,** 1–25 (2020).

73. Bubb, E. J., Metzler-Baddeley, C. & Aggleton, J. P. *The cingulum bundle: Anatomy, function, and dysfunction* 2018.

74. Shahbaba, B. *et al.* Hippocampal ensembles represent sequential relationships among an extended sequence of nonspatial events. *Nature Communications* **13,** 1–17 (2022).

75. Eichenbaum, H. *Time cells in the hippocampus: A new dimension for mapping memories* 2014.

76. Simonnet, J. *et al.* Activity dependent feedback inhibition may maintain head direction signals in mouse presubiculum. *Nature Communications* **8,** 1–14 (2017).

77. Voigts, J. & Harnett, M. T. Somatic and Dendritic Encoding of Spatial Variables in Retrosplenial Cortex Differs during 2D Navigation. *Neuron* **105,** 237–245.e4 (2020).

78. Pachitariu, M. *et al.* Suite2p: beyond 10,000 neurons with standard two-photon microscopy. *bioRxiv,* 061507 (2016).

79. Stringer, C. & Pachitariu, M. Computational processing of neural recordings from calcium imaging data. *Current Opinion in Neurobiology* **55,** 22–31 (2019).

80. Friedrich, J., Zhou, P. & Paninski, L. Fast online deconvolution of calcium imaging data. *PLoS Computational Biology* **13,** e1005423. arXiv: `1609.00639` (2017).

81. Xu, Z. *et al.* A Comparison of Neural Decoding Methods and Population Coding Across Thalamo-Cortical Head Direction Cells. *Frontiers in Neural Circuits* **13,** 75 (2019).

Figures

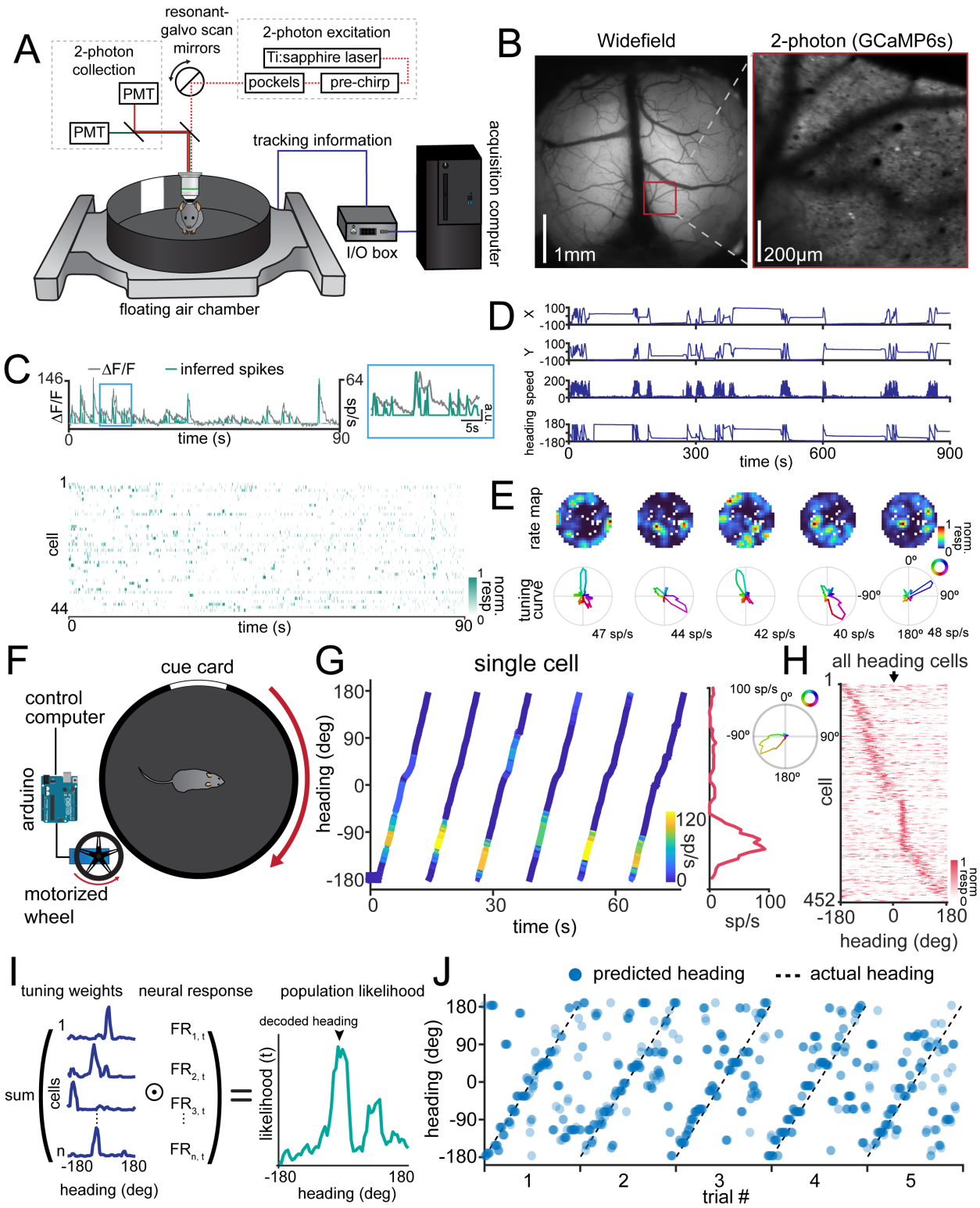

Figure 1: Individual neurons in the RSC exhibit heading responses in the absence of physical head movement.

A) Schematic of the imaging set up. Mice are head fixed in a floating chamber and allowed to voluntarily

move the chamber floor using their paws, allowing control of their position and orientation within the chamber. Tracking information from the chamber is synchronized to the collection of the two-photon image acquisition.

B) *Left:* Example widefield image of the entire cortical window with the location of the imaged plane in dysgranular RSC indicated with a red box. Scale bar = 1 mm. *Right:* Example imaging plane in RSC using two-photon microscopy. Scale bar = 200 μm.

C) *Top:* Neural responses are first extracted as changes in fluorescence ($\Delta F/F$), then spikes are inferred from the calcium traces. Gray traces show the $\Delta F/F$ trace and the green trace shows the inferred spikes. *Inset:* Zoomed section of the blue box on the left. *Bottom:* Example inferred spikes from a population of cells in a single recording.

D) Example chamber tracking data from a single experiment, showing X position, Y position, speed, and heading angle.

E) Example rate maps (top) and tuning curves (bottom) from neurons recorded from RSC. Note that neurons exhibit selectivity to heading, but not to allocentric position.

F) Schematic of the controlled rotation set up. A motorized wheel is added to control the rotation of the floating cage. The mouse is head-fixed in the center of the chamber and the X-Y translation of the chamber is limited by guide bars. The red arrows show the rotation of the wheel and chamber.

G) *Left:* Example of a single neuron's response to rotation in the chamber. The orientation of the chamber ("heading") is plotted against time, and the activity represented by the line color as indicated in the inset colorbar. The neuron consistently responds at the same heading across trials. *Right:* Average tuning curve across all trials, showing the elevated response of the neuron at a specific heading. *Inset:* The same tuning curve plotted in polar coordinates.

H) Tuning curves of all responsive neurons, sorted by cross-validated angle of peak response, showing that the preferred headings of the population spans the entire floating chamber.

I) Schematic of the decoding method. Each cell's tuning curve is used as a weight vector and is multiplied against its current activity rate to create a population likelihood curve for each time bin (t) (see Methods). The decoded heading is the peak of the likelihood curve. $\odot$ represents elementwise multiplication.

J) Decoding of heading from population responses from a single recording. Predicted headings for individual 100 ms time bins are plotted as blue dots. The actual heading is plotted as a dotted black line.

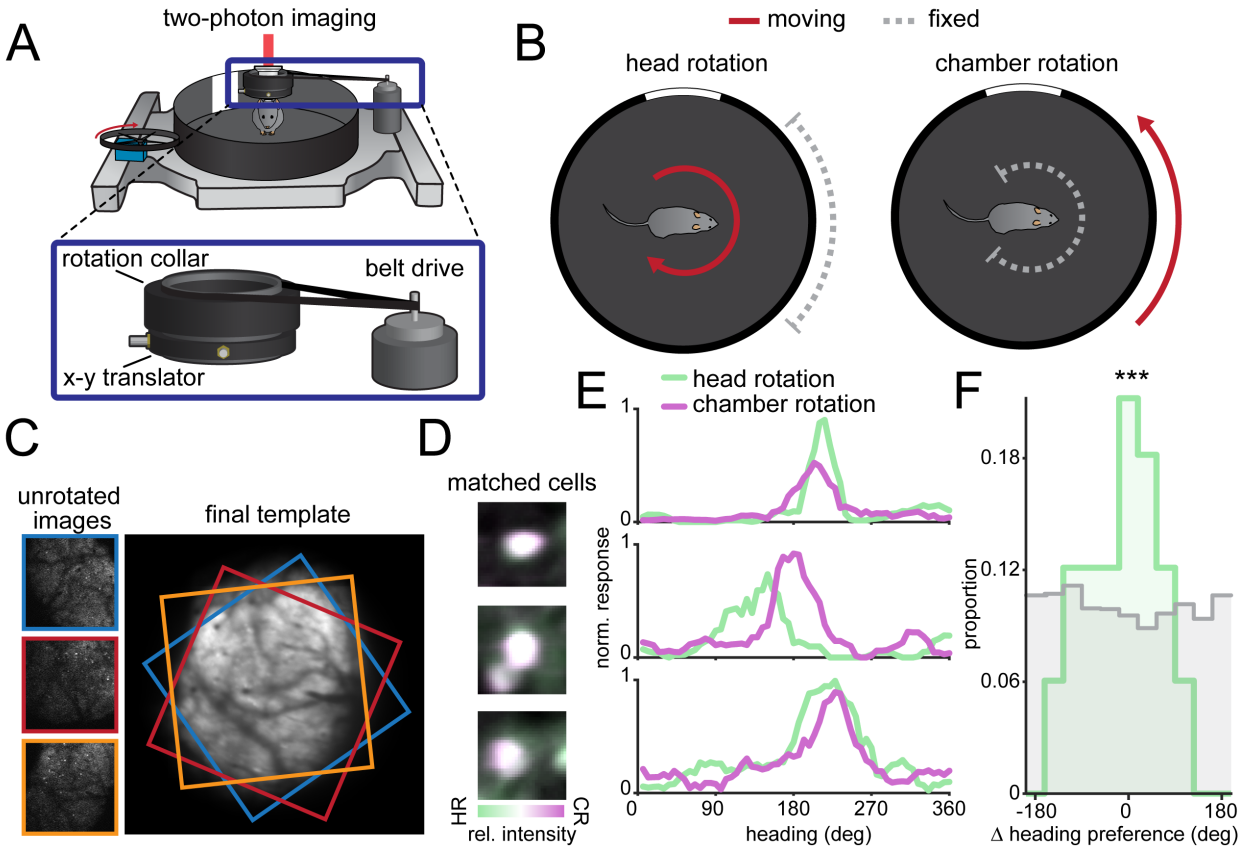

Figure 2: Neurons in the RSC retain similar tuning in head-rotation or chamber-rotation conditions.
A) Example of the adapted head-rotation set up for comparisons between head-rotation and chamber-rotation experiments. In addition to the motor-driven wheel that can rotate the chamber while the head is immobilized, there is a separate rotation collar that can be used to rotate the mouse over the stationary chamber. *Inset:* Zoom in of the rotation collar assembly. The rotation collar contains an x-y translator to shift the axis of rotation to the center of the imaging field. A belt-drive connects the collar to a motor for controlled rotation.
B) Schematic of the two experimental conditions. Either the chamber or the head rotates independently, shown with a red arrow, while the other remains stationary, shown with a dashed gray capped line. In both cases, this causes the visual cue card to move across the visual field in the same direction.
C) Example of derotation process for image timeseries. Each of the three raw images is rotated to match the template on the right. Colored borders show the position and rotation of each individual image. The final template shown on the right is after all the images have been registered for the recording.
D) Example of three matched ROIs from the recordings. Purple denotes greater brightness in the chamber-rotation recording, whereas green denotes greater brightness in the head-rotation recording. White denotes equal brightness and suggests good alignment of the ROIs across recordings. HR: Heading rotation, CR: chamber rotation
E) Three example tuning curves from pairs of ROIs showing similar tuning preferences. The tuning curve in the head rotation condition is shown in green, whereas the tuning curve in the chamber rotation condition is shown in purple.
F) Histogram showing the difference in peak heading preference across recordings for matched ROIs. The zero-centered peak in the data (green) indicates that cells remained tuned to the similar heading angles independent of head- or chamber-rotation. Shuffled distribution is shown in gray. ***: $p < 0.001$, V-test for circular nonuniformity against 0°.

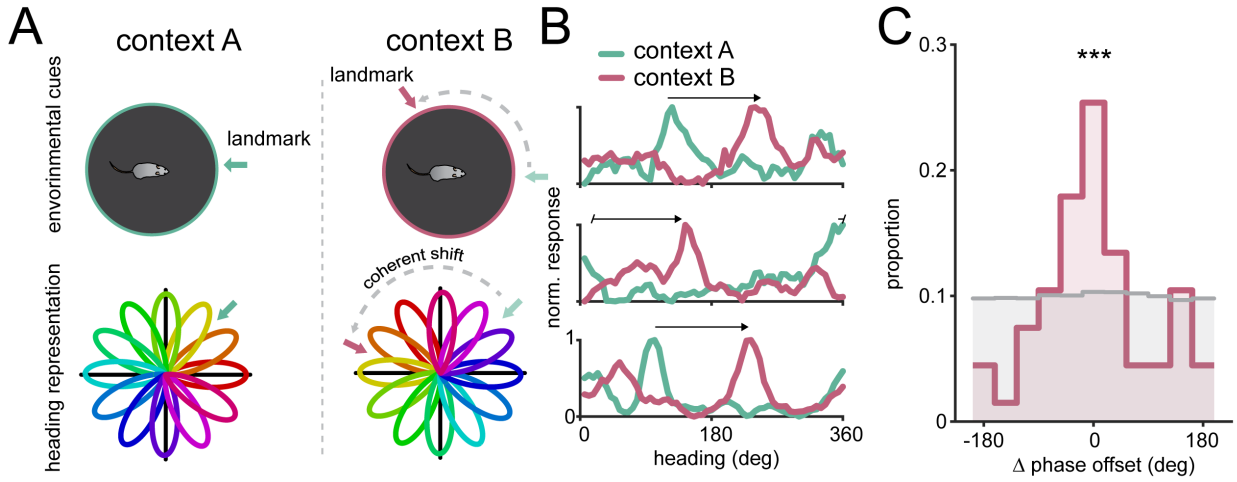

Figure 3: The heading network coherently remaps when visual cues are changed.
A) Schematic showing coherent remapping across two different contexts. Because each individual neuron's preferred heading is mapped as a relative offset to visual landmarks, the relationships between neuron offsets would be expected to be preserved across contexts, leading to a coherent population shift.
B) Three example neurons showing a unified shift in preferred heading from context A to context B. Tuning curve from context A is shown in green, while tuning curve from context B is shown in purple. Arrow shows the phase offset between contexts.
C) Histogram showing that neurons coherently remap across conditions. For each recording session, a neuron's coherence with the population was calculated as the difference between the neuron's degree of remapping and averaged degree of remapping across the remainder of the population (see Methods). The peak around 0 suggests in the real data (purple) shows that individual neurons are shifting preferred directions in a similar amount to the rest of the population in each recording. Shuffled distribution is shown in gray. ***: $p < 0.001$, V-test for circular nonuniformity against 0°.

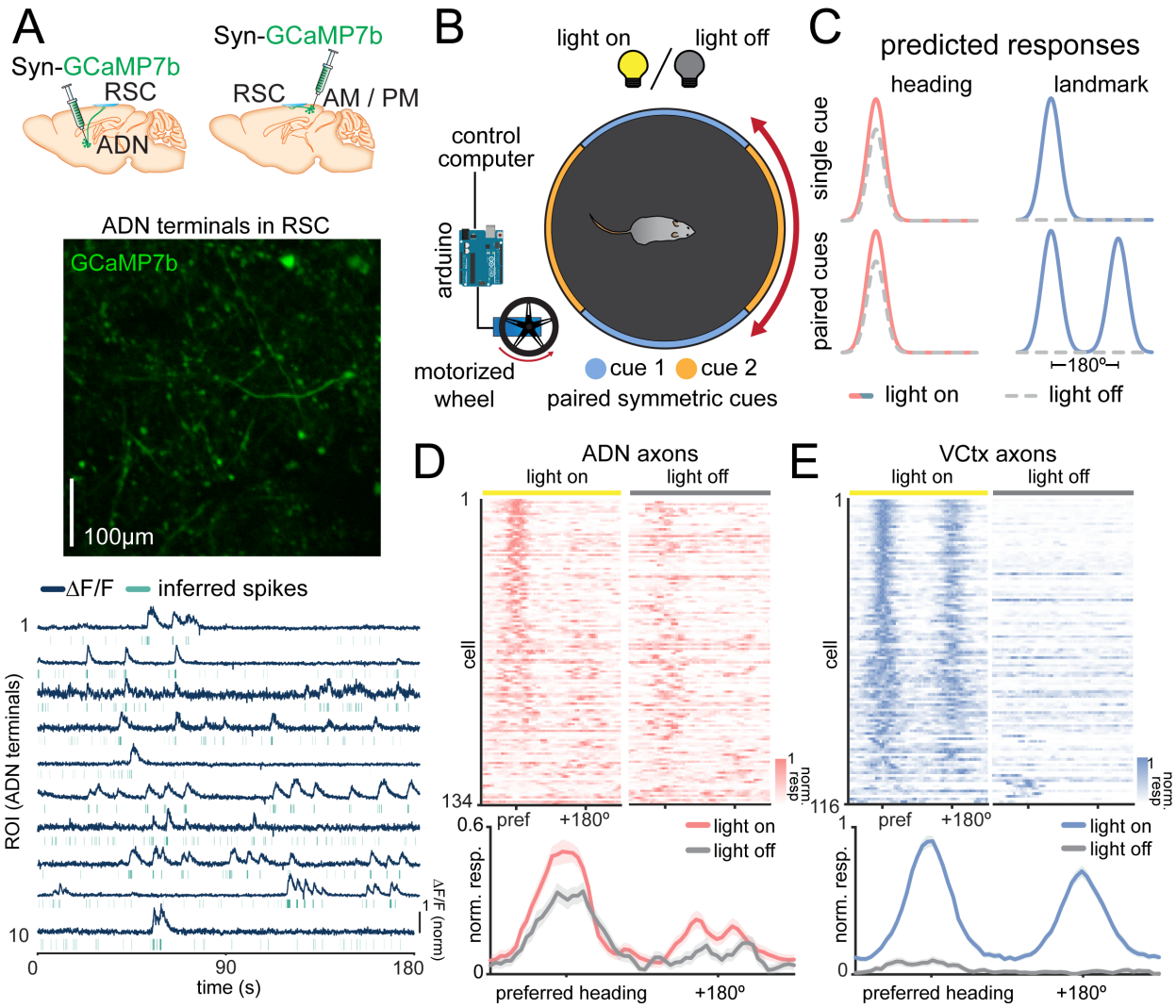

Figure 4: Imaging projections from ADN and visual cortex reveal distinctly tuned responses sent to RSC. **A)** *Top:* Example of injection sites in separate cohorts of mice. AAV-Syn-GCaMP7b was injected into either ADN or AM/PM of WT mice. *Middle:* Example imaging field in RSC of axon terminals originating from ADN. *Bottom:* Example $\Delta F/F$ traces and inferred spikes for imaged ADN terminals it RSC.
B) Example schematic of experimental conditions. The single white cue card has been replaced with paired symmetric cues on the floating chamber, which is driven by a motorized wheel. Neurons from RSC are recorded across light-on and light-off phases.
C) Schematic of expected axonal responses. *Left:* Axons terminals encoding heading independent of visual cues are expected to have unimodal tuning curves across both conditions that are not affected by the light condition. *Right:* Axons terminals responding to visual cues are expected to show a single peak in a single-cue condition, but dual peaks in the paired symmetric cue condition. In both cases, the responses will be reduced in the light-off condition.
D) Responses of ADN axons across recordings. *Top:* Heat maps in the light-on (left) and light-off (right) condition. Each row represents the aligned response of a single axon, and axons are organized by similarity to a group mean in the light-on condition. *Bottom:* Averaged response across all ADN axons, showing an aligned unimodal peak in both light-on and light-off conditions. Traces shown are mean ± s.e.m.a
E) Same as **D**, but for visual cortex axons. Averaged response shows a bimodal peak in the light-on condition, and no response in the light-off condition.

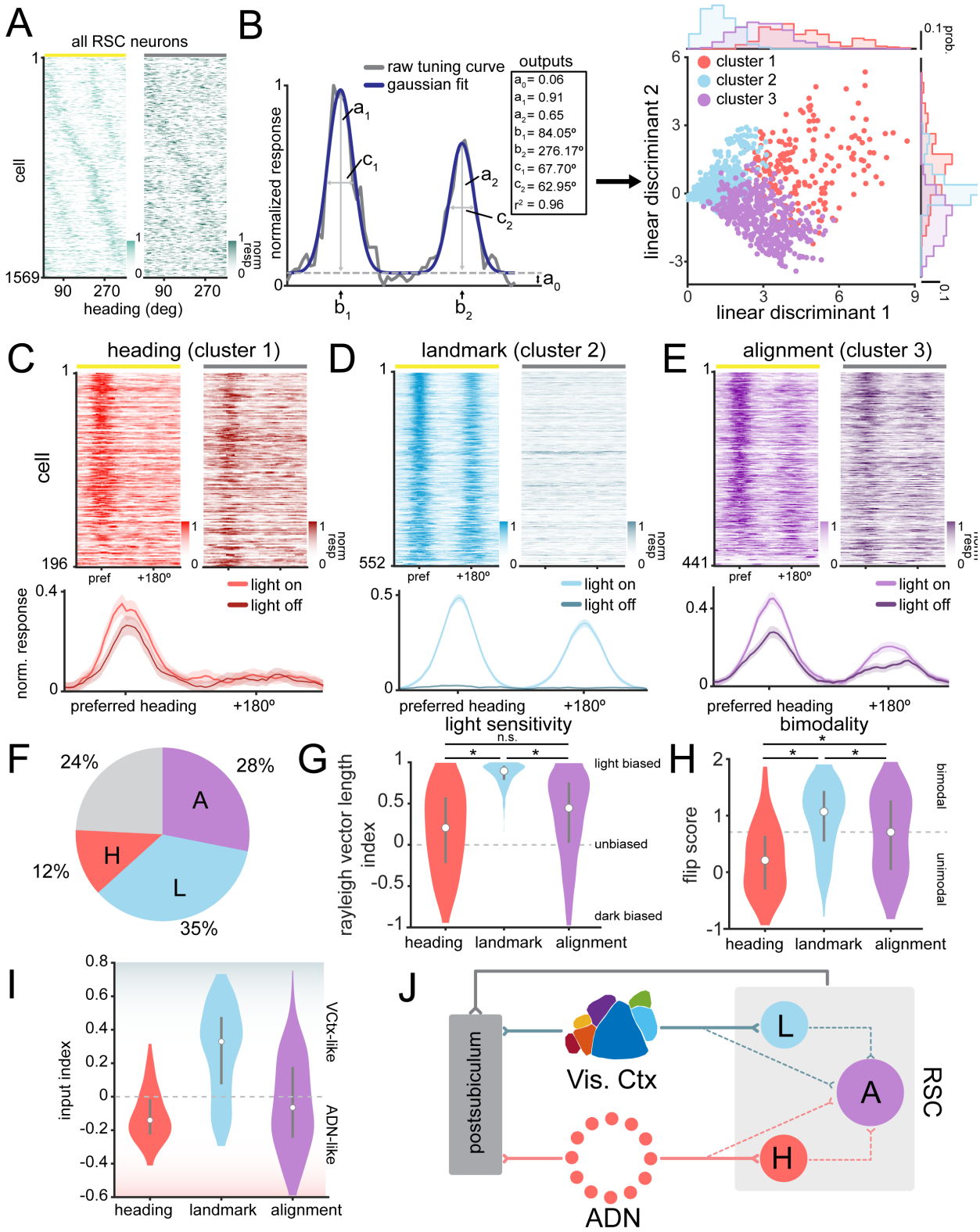

Figure 5: Unsupervised clustering of neural responses in the RSC reveals distinct functional classes. **A)** Heat maps of the responses of all somas imaged in RSC. Each row corresponds to a neuron in the light-on and light-off condition, and responses are ordered by their preferred direction. Light-off responses are ordered based on their light-on position.

B) *Left:* Example of a two-term Gaussian fit on an aligned and normalized tuning curve. The outputs of the two-term Gaussian for light-on and light-off conditions are used for clustering. *Right:* Scatter plot of clustered responses in a reduced dimension (LDA space). Histograms along the edges show the distribution of values along each dimension. Cluster numbers are denoted by color. Note that LDA plot is only for visualization, clustering was performed in full 8-dimensional space (see Methods).
C) *Top:* Heatmaps showing the aligned responses of the heading neurons (cluster 1), ordered by similarity to a cluster averaged response. *Bottom:* Average responses of the neurons in the heading cluster in light-on and light-off conditions. Traces are shown as mean ± s.e.m.
D) Same as **C**, but for landmark neurons (cluster 2).
E) Same as **C**, but for alignment neurons (cluster 3).
F) Pie chart showing the proportion of cells in each cluster. Unclassified cells (gray) were defined as cells that were dissimilar from any of the cluster averages (see Methods). H: Heading cells, L: Landmark cells, A: Alignment cells
G) Distributions of light sensitivity across cell types, calculated as an index based on the light-on and light-off Rayleigh vector length (see Methods). Center dot is the median and bars span from 25th to the 75th percentile.
H) Distributions of bimodality across cell types, calculated based on the flip score (see Methods). Center dot is the median and bars span from 25th to the 75th percentile.
I) Distributions of input index across cell types (see Methods). Center dot is the median and bars span from 25th to the 75th percentile.
J) Proposed model of connectivity for visual information integration into the heading network. Dotted lines suggest putative projections.
*: non-overlapping 95%CI

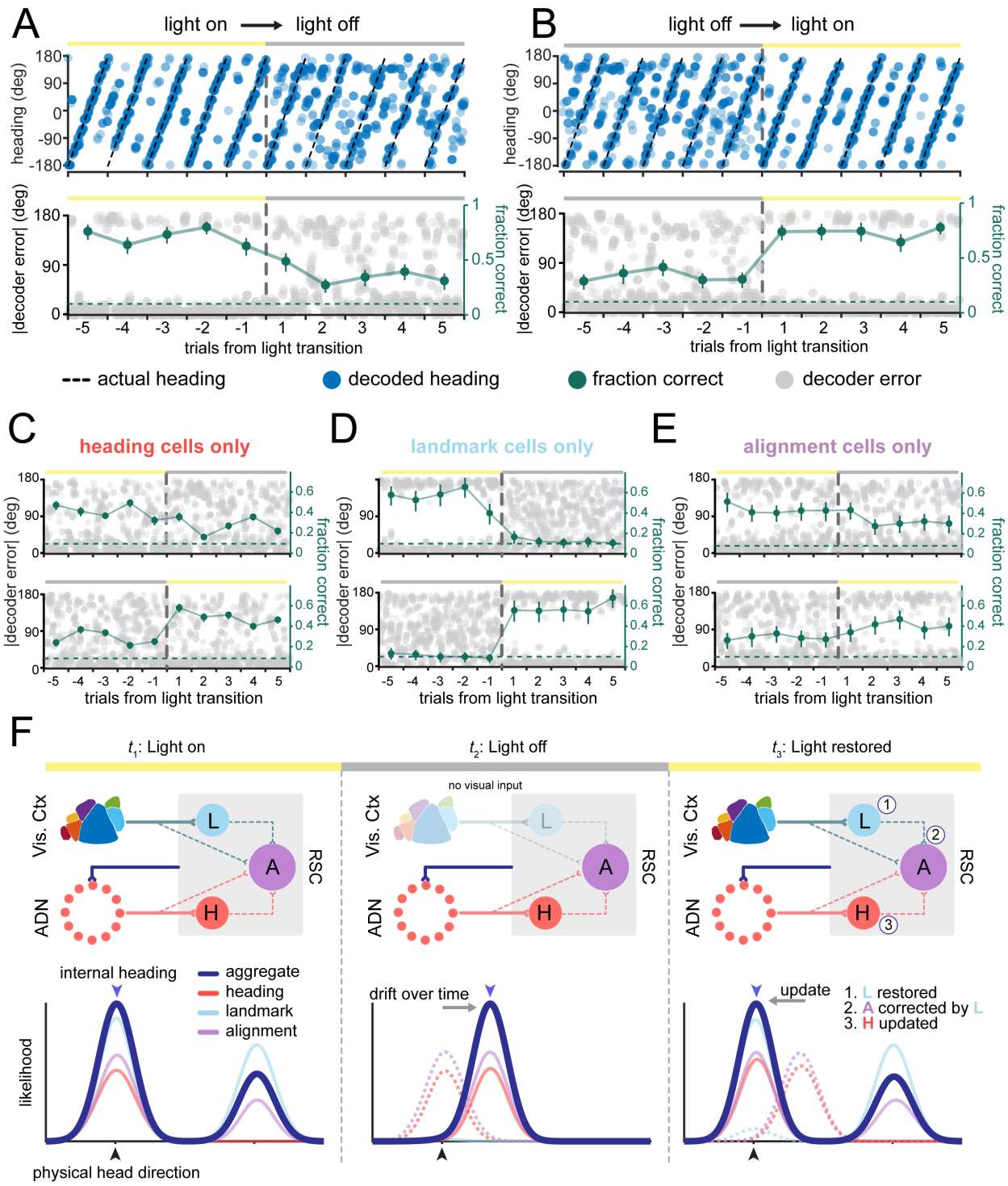

Figure 6: Decoding analysis shows independent contributions of each functional subclass to the overall heading representation in RSC.

A) Pseudopopulation decoding of neural responses across trials. *Top:* Predicted heading plotted for each 100 ms time bin (blue dots) overlaid on actual heading (black dotted line) for each trial, transitioning from the light-on (yellow bar) to the light-off (gray bar) condition. The transition line between conditions is shown as a vertical gray dashed line. *Bottom:* Decoder error (gray dots) and the average fraction correct for each trial (green dots and line) plotted as a function of trial relative to light-on to light-off transition. The dashed

green line denotes chance level for fraction correct (0.18). Fraction correct is plotted as mean ± s.e.m.
B) Same as **A**, but for light-off to light-on transition.
C) *Top:* Decoder error (gray dots) and fraction correct (green dots and line) for decoder using only heading cells in light-on to light-off transition. *Bottom:* Same as top, but for light-off to light-on transition.
D) Same as **C**, but for landmark cells only.
E) Same as **C**, but for alignment cells only.
F) Schematic of circuit for integration of visual information into the HD network, indicating changes in circuit representation during light-on condition (left), light-off condition (middle), and back in the light-on transition (right). *Top:* The blue feedback line describes putative feedback from the RSC to the ADN, sending adjusted heading information. *Bottom:* Population likelihood curves are shown in dark blue, with each cell class (heading, landmark, and alignment) shown in red, blue, and purple, respectively. Blue arrows above the likelihood curves denote the predicted internal heading at each time point. Black arrows below the likelihood curves denote the physical head direction at each time point. Dotted lines denote the previous position of the likelihood curve.

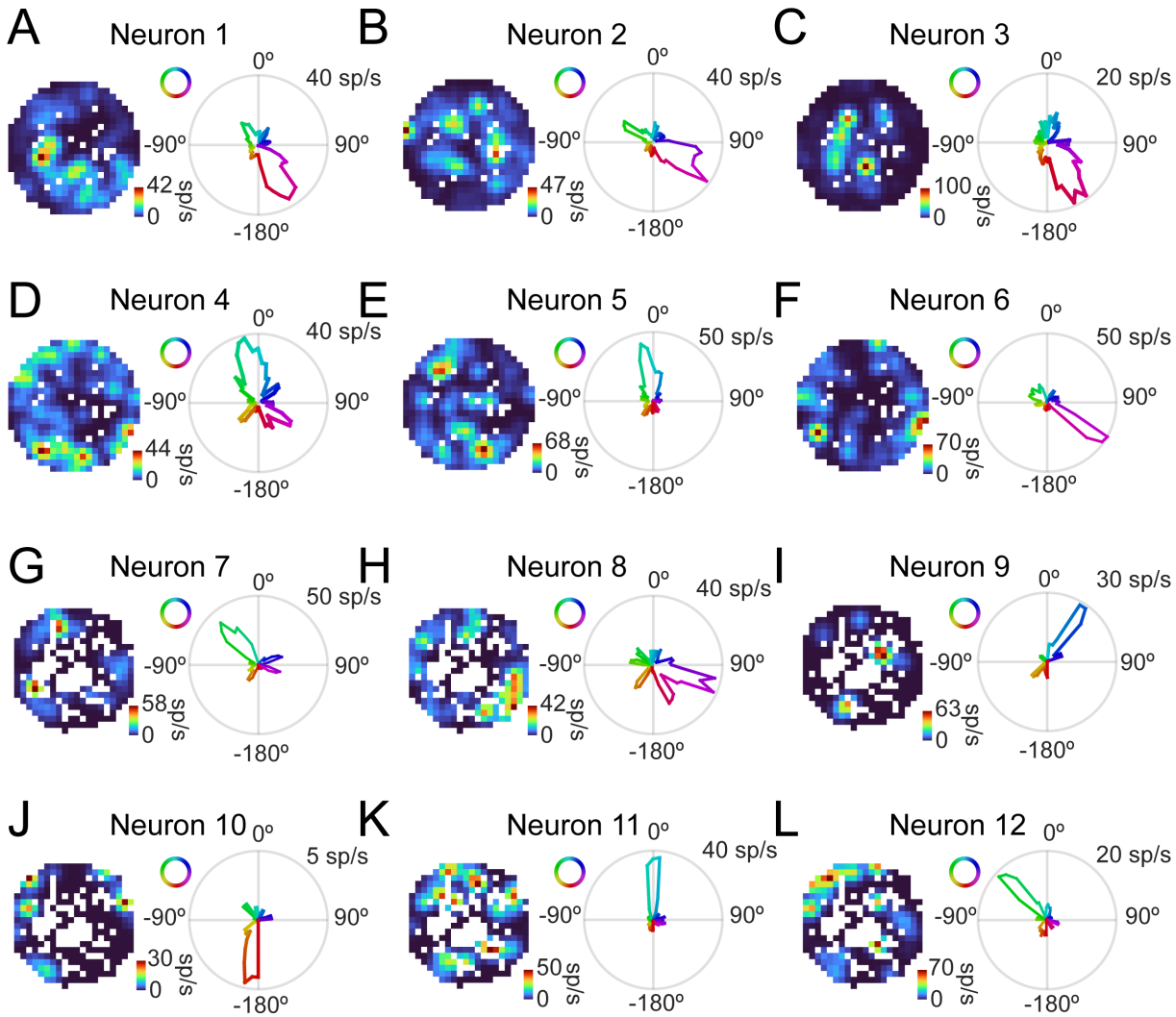

Figure S1: RSC neurons represent heading during locomotion in the floating chamber.
A) *Left:* Example spike rate heat map of a single neuron, showing the neuron's response as chamber moves around the mouse. *Right:* Example tuning curve from the same neuron.
B-L) Same as **A** for additional example neurons.

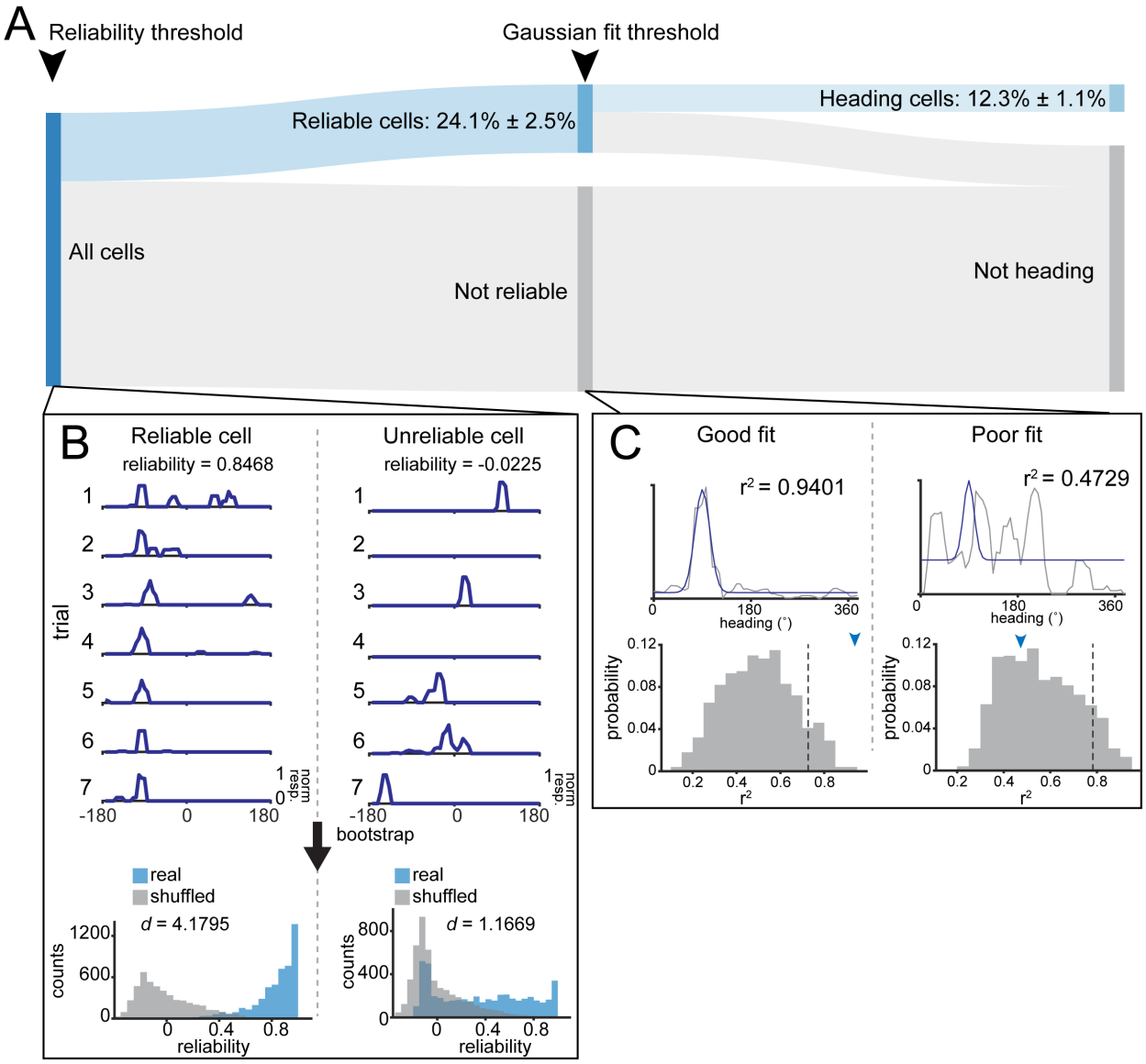

Figure S2: Schematic of procedure for determining whether a cell is heading responsive.
A) Sankey diagram showing the percentage of cells passing each selection criteria for determining heading responsiveness. All cells first pass through a reliability threshold, followed by a Gaussian fit threshold. Both thresholds were calculated via a shuffling procedure (see Methods). Only cells which pass both thresholds were included in analyses.
B) Schematized reliability threshold using an example cell. *Left:* Trial-by-trial tuning curves for a reliable neuron showing a prominent peak in the same location over trials. Below are histograms comparing bootstrapped reliability of this cell versus a shuffled distribution. *Right:* Same as *left*, but for an unreliable cell.
C) Schematized procedure for Gaussian fit threshold. *Left:* Cells are fit with a single term Gaussian. A shuffled distribution of r^2 is created by circularly shifting tuning curves from each trial (see Methods). The distributions of r^2 are shown with a dotted line denoting the 99th percentilie and the blue arrow showing the reliability of the current cell. *Right:* Same as *left*, but for a poorly fit cell.

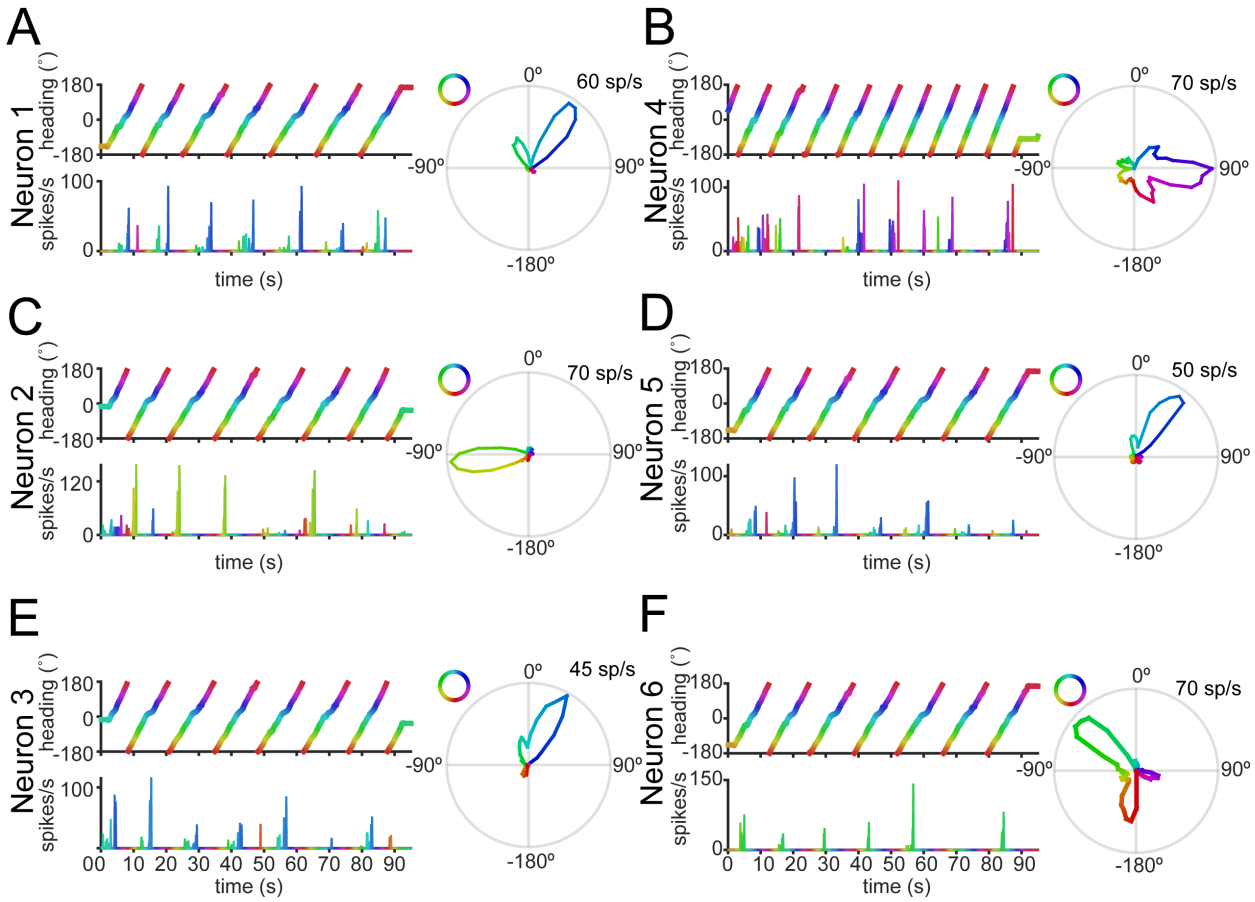

Figure S3: Neurons in the forced rotation condition represent heading faithfully over multiple trials. **A)** *Left, top:* Recorded heading over time, color coded by the current heading. *Left, bottom:* An example neuron's spike rate over the same duration, with the color of the line matched to the heading shown above. The similar color of the peaks show that the neuron is responding to the same heading on each trial. *Right:* Tuning curve from the example neuron.
B-F) Same as **A** for additional example neurons.

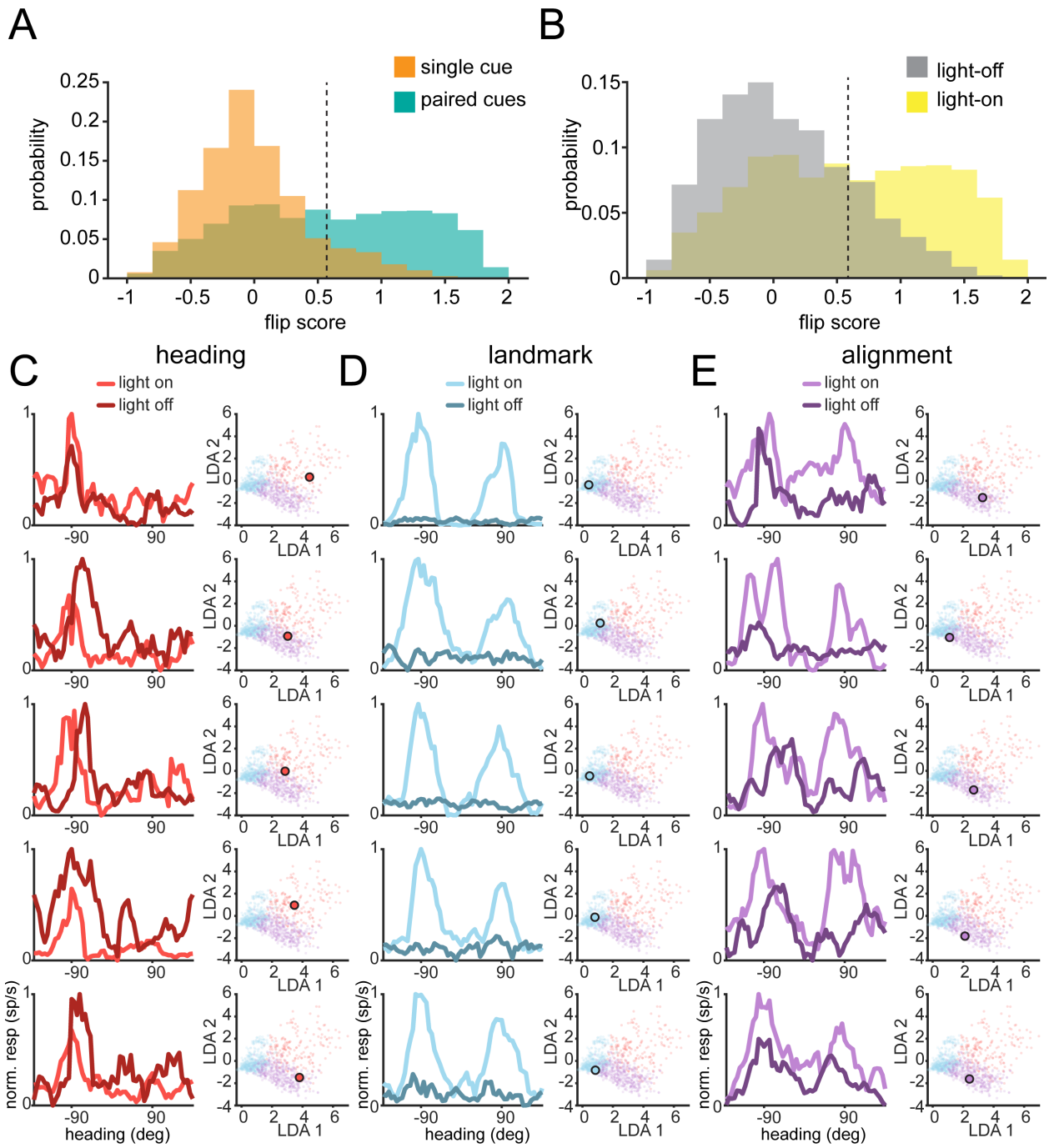

Figure S4: Neurons in the RSC have responses that cluster into three distinct profiles.
A) Histogram of flip scores between the single cue experiments (orange, Figure 1) and paired cue experiments (green).
B) Histogram of flip scores in the paired cue experiments comparing light-on (green) and light-off (gray) conditions.
C) Example aligned tuning curves for heading cells, next to their position on the reduced dimensional space scatter plot. Each cell's position is shown with a large outlined dot.
D) Same as **A**, but for landmark cells.
E) Same as **A**, but for alignment cells.

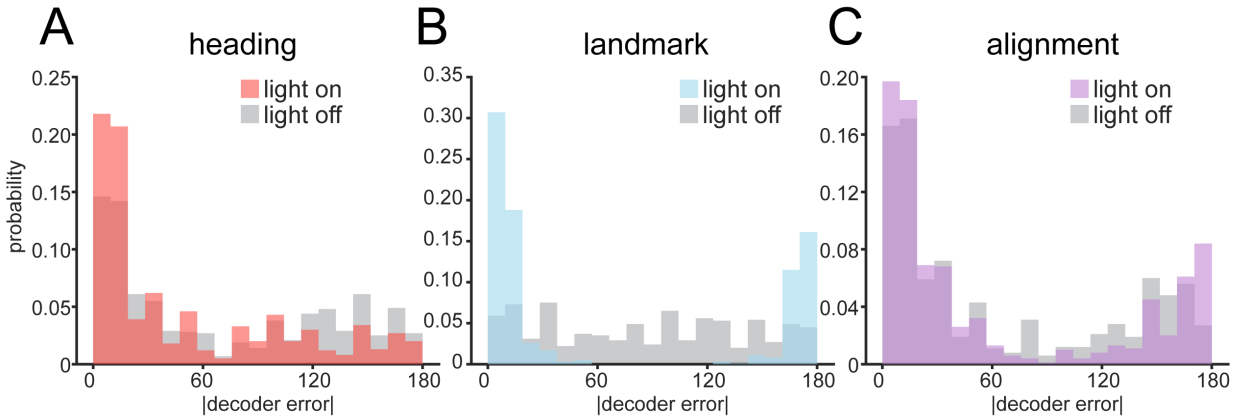

Figure S5: Histograms of decoder error reveal the preponderance of 180°errors in decoding landmark and alignment, but not heading, cells.
A) Example histograms of decoder error in light-on and light-off conditions for heading cells only.
B) Same as **A**, but for landmark cells.
C) Same as **A**, but for alignment cells.